10.1161/CIRCULATIONAHA.118.033794

FTO-Dependent m6A Regulates Cardiac Function During Remodeling and Repair

Running Title: *Mathiyalagan et al.; FTO-Dependent m6A Regulates Cardiac Function*

Prabhu Mathiyalagan, PhD; Marta Adamiak, PhD; Joshua Mayourian, PhD; Yassine Sassi, PhD; Yaxuan Liang, PhD; Neha Agarwal, MS; Divya Jha, PhD; Shihong Zhang, BS; Erik Kohlbrenner, BS; Elena Chepurko, DVM; Jiqiu Chen, MD; Maria G. Trivieri, MD; Rajvir Singh, PhD; Rihab Bouchareb, PhD; Kenneth Fish, PhD; Kiyotake Ishikawa, MD, PhD; Djamel Lebeche, PhD; Roger J Hajjar, MD; Susmita Sahoo, PhD

Cardiovascular Research Center, Icahn School of Medicine, Mount Sinai, NY

Address for Correspondence:
Susmita Sahoo, PhD
Cardiovascular Research Center
Icahn School of Medicine at Mount Sinai
One Gustave L. Levy Place, Box 1030
New York, New York 10029-6574
Tel: 212.824.8913
Fax: 212.241.4080
Email: susmita.sahoo@mssm.edu

Abstract

Background—Despite its functional importance in various fundamental bioprocesses, the studies of N6-methyladenosine (m6A) in the heart are lacking. Here we show that, fat mass and obesity-associated (FTO), an m6A demethylase, plays a critical role in cardiac contractile function during homeostasis, remodeling and regeneration.

Methods–We used clinical human samples, preclinical pig and mouse models and primary cardiomyocyte cell cultures to study the functional role of m6A and FTO in the heart and in cardiomyocytes. We modulated expression of FTO using AAV9 (in vivo), adenovirus (both in vivo and in vitro) and siRNAs (in vitro) to study its function in regulating cardiomyocyte m6A, calcium dynamics and contractility and cardiac function post-ischemia. We performed methylated (m6A) RNA immunoprecipitation sequencing (MeRIP-seq) to map transcriptome-wide m6A, and MeRIP qPCR assays to map and validate m6A in individual transcripts, in healthy and failing hearts and myocytes.

Results–We discovered that FTO has decreased expression in failing mammalian hearts and hypoxic cardiomyocytes, thereby increasing m6A in RNA and decreasing cardiomyocyte contractile function. Improving expression of FTO in failing mouse hearts attenuated the ischemia-induced increase in m6A and decrease in cardiac contractile function. This is carried out by the demethylation activity of FTO, which selectively demethylates cardiac contractile transcripts, thus preventing their degradation and improving their protein expression under ischemia. Additionally, we demonstrate that FTO overexpression in mouse models of MI decreased fibrosis and enhanced angiogenesis.

Conclusions–Collectively, our study demonstrates the functional importance of FTO-dependent cardiac m6A methylome in cardiac contraction during heart failure and provides a novel mechanistic insight into the therapeutic mechanisms of FTO.

Key Words: m6A; FTO; myocardial ischemia; RNA methylation; heart failure

Clinical Perspective

What is new?

- We discovered that m6A, one of the most prevalent and functionally relevant RNA modifications, is increased in failing mammalian hearts and in hypoxic cardiomyocytes.
- Our research suggests that dysregulation of m6A is an important hallmark of mammalian heart failure.
- Expression of an m6A demethylase, FTO (Fat-mass and obesity associated protein) decreases in failing hearts leading to aberrant increase in transcriptome-wide m6A and decreasing cardiomyocyte contractile function.
- Improving expression of FTO in ischemic mouse hearts attenuates ischemia-induced increase in m6A and decrease in cardiac contractile function. FTO selectively demethylates cardiac contractile transcripts, thus preventing their degradation and improving their protein expression under ischemia.

What are the clinical implications?

- Our study demonstrates the functional importance of FTO-dependent cardiac m6A methylome in cardiac contraction during heart failure and provides a novel mechanistic insight into the therapeutic mechanisms of FTO.
- Our data provides proof of principle that FTO plays important functional role in cardiac homeostasis and myocardial repair and that targeting FTO signaling may represent a promising therapeutic strategy to treat heart failure.
- Our findings on the dynamic nature of the cardiac m6A-epitranscriptome lead to deeper understanding of the mechanism of cardiac remodeling on one hand and innovative therapeutic interventions on the other.

Introduction

Current therapeutic approaches have resulted in limited success in treating ischemic heart disease and mitigating post-ischemic adverse cardiac remodeling. Therefore, new concepts for myocardial repair and regeneration that improves cardiac function have to be developed. While several transcription factors and transcriptional co-activators have been studied in the context of heart failure, post-transcriptional regulations of cardiac mRNAs that can affect expression of key proteins and cardiac function remain largely unexplored. Earlier studies have shown that i) protein expression in failing human hearts does not correlate with the corresponding mRNA abundance [1, 2], and ii) nuclear and cytosolic mRNA levels do not correlate in cardiac myocytes [3], suggesting a role for altered post-transcriptional RNA modifications in regulating protein expression in failing hearts. Therefore, we investigated epitranscriptomic regulations underlying cardiac remodeling and found a predominant but previously unidentified mechanism contributing to heart failure via dysregulated RNA modifications.

Even though epitranscriptomic mechanisms are under intense study, our knowledge about its biological function, especially in healthy tissues, organs and under pathological conditions are limited. Recent findings suggest that the most abundant internal chemical modification in RNA, N6-methyladenosine (m6A) is a critical regulator of mRNA stability, protein expression and several other cellular processes [4-7]. While dysregulated m6A has been linked to various types of cancers [8, 9] and brain diseases [10], its role in cardiac homeostasis and failure has not been studied.

Several recent discoveries suggest that epitranscriptomic mRNA modifications are reversible and dynamically regulated with dedicated writers (methyltransferases) that catalyze addition of m6A (METTL3, METTL4, METTL14 and WTAP) and dedicated erasers (demethylases) that catalyze removal of m6A (FTO, ALKBH5) from mRNA [11]. The fat mass and

obesity-associated (FTO) protein has been found to have a key role in regulating transcriptome-wide m6A modification in mRNA [4, 12] and is one of the m6A regulators that has been associated with metabolic disorders such as diabetes and obesity [13, 14]. Although FTO is expressed ubiquitously, cardiac ventricular levels are high in addition to brain and liver tissues in human embryos [15]. Interestingly, FTO has been implicated in cardiac defects including hypertrophic cardiomyopathy, ventricular septal and atrio-ventricular defects [15], arrhythmias [16] and coronary heart disease [17] suggesting an important role for FTO in ischemic heart failure.

So far, m6A function in physiological and biological processes have been investigated. However, studies of m6A under pathological conditions, especially in tissues and organs are limited. Moreover, FTO-dependent m6A demethylation and its role in cardiac protein expression and contractility in healthy and failing myocardium have not been addressed. Using clinical human samples, preclinical pig and mouse models of heart failure and primary cardiomyocyte cell culture, we have investigated the physiological and pathological role of FTO-dependent m6A epitranscriptome in cardiac homeostasis, remodeling and repair. We present evidence that m6A in RNA is dysregulated in failing hearts and that FTO-dependent m6A plays a significant role in pathomechanisms of heart failure at the molecular (mRNA degradation and protein expression), cellular and organ (cardiomyocyte and cardiac function) levels. Moreover, we show that FTO gene delivery attenuates the ischemia-induced cardiac remodeling demonstrating the therapeutic potential of FTO in the treatment of heart failure. Mechanistically, FTO selectively demethylates calcium handling and contractile transcripts, preventing their degradation and regulating their protein expression in the failing heart. Our results have uncovered a novel function for FTO-regulated m6A mechanisms in cardiac remodeling and repair. We also establish that targeting cardiac epitranscriptome via FTO can be an effective therapeutic strategy for heart failure.

Methods

The data, analytic methods, and study materials will be made available to other researchers for purposes of reproducing the results or replicating the procedure.

Study design

Human left ventricular (LV) tissues were obtained from deidentified, postmortem failing (with diagnosed cardiomyopathy) and non-failing (with no history of cardiomyopathy and non-cardiac related death) hearts from National Disease Research Interchange (NDRI). No human subjects were involved. Mount Sinai Institutional Review Board approved procurement of human tissue samples from NDRI and all usage was done as per Mount Sinai approved guidelines. Both male and female tissues were used from human failing and non-failing hearts. Similarly, for all animal experiments, both male and female mice (c57Bl6) and rats (Sprague-Dawley rats for cardiomyocyte isolation) were used. All the experimental protocols are in compliance with the National Institutes of Health Guide for the Care and Use of Laboratory Animals and standards of United States regulatory agencies. All treatments and measurements of cardiomyocyte (Ionoptix) and cardiac (echocardiography) function were performed in a blinded manner. To investigate m6A in cardiac transcriptome, we developed novel methods such as m6A quantification in total or polyA$^+$ RNA and methylated (m6A) RNA immunoprecipitation and sequencing (MeRIP-seq) in RNA isolated from mouse and human cardiac tissues. m6A-related new protocols are described here. Rest of the methods are described in detail in the Online-only Data Supplement.

PolyA$^+$ RNA isolation from human and mouse LV

For human polyA$^+$ RNA, ~100mg of LV tissue was homogenized using multiple RNase/DNase free 2 ml lysing matrix tubes (MP Biomedicals) using tissue homogenizer. For mouse polyA$^+$ RNA isolation, 3-4 sham or 5-6 MI (infarct) LV tissues were pooled to achieve ~100mg tissue

and homogenized as described for human samples. RNA was extracted using miRNAeasy kit (Qiagen) as recommended by manufacturer (more detail in Online Supplement). For polyA$^+$ RNA isolation, ~150ug of total RNA in 500ml RNAse-free water from each LV extract was then pre-warmed in a 65^{o}C-heating block for 10 minutes before adding Biotinylated-Oligo (dT) probe for hybridization (Promega). After allowing Oligo-(dT) hybridization to poly(A) tail for 10 minutes in room temperature, Streptavidin-Paramagnetic Particles (Promega) were added and polyA$^+$ containing RNA was isolated using magnetic capture of biotin-streptavidin conjugates. PolyA$^+$ RNA was then eluted in RNase-free water as recommended by the manufacturer's protocol. The isolation of polyA$^+$ RNA fraction was ensured by analyzing polyA$^+$ RNA in a bioanalyzer. PolyA$^+$ RNA was immediately quantified using nanodrop spectrophotometer and RNA samples were stored as aliquots at -80^{o}C.

Quantification of m6A in total and polyA$^+$ RNA

Column purified total RNA (miRNeasy, Qiagen) or Oligo-dT enriched polyA$^+$ RNA (Promega) was used for quantification of m6A modification. For quantification of m6A in human, pig and mouse failing or non-failing ischemic LV, we used previously described antibody-based m6A capture and colorimetric quantification method (P-9005, EpiGentek)[18, 19]. For both total or polyA$^+$ RNA, 200ng of RNA per sample was transferred to corresponding wells in a 96-well plate. All samples were performed in duplicates. Both negative and positive controls as well as a standard curve in the range of 0.02ng to 1ng of m6A were included as recommended by the manufacturer. Briefly, after binding of RNA to wells, anti-m6A antibody was added and washed three to four times as recommended by manufacturer's protocol. Antibody bound m6A in RNA was detected by adding developer solution and colorimetric quantification was carried out subsequently using SpectraMax plus microplate reader. Percentage of m6A in RNA was

calculated and compared to corresponding control samples and established as % m6A in total RNA.

Methylated RNA immunoprecipitation and next generation sequencing (MeRIP-seq)

Briefly, 200ug of human or mouse total RNA was used. For mouse, at least 4 LVs per sham group and at least 6 LVs per MI group were pooled to achieve 200ug of RNA (RIN>8). Both human and mouse total RNA were then isolated for polyA$^+$ RNA (Promega) and RNA quantified. PolyA$^+$ RNA was then fragmented to ~100nt long fragments using RNA fragmentation buffer (Millipore Sigma). RNA fragmentation was ensured by bioanalyzer before proceeding to m6A-IP. Non-IP RNA was stored from fragmented RNA for bioinformatics analysis. The remaining fragmented polyA$^+$ RNA was subjected to m6A-IP using 5ug of anti-M6A (17-10499, Millipore Sigma)[20]. Antibody bound m6A-modified RNAs were eluted in RNase-free water as recommended by the manufacturer's protocol. Immunopurified RNA was then precipitated overnight at 4^{o}C and samples were sent to Weill Cornell Medical College Genomic Core facility (New York) for library construction. The usual steps involving polyA$^+$ enrichment and fragmentation during library construction were omitted and libraries were constructed using RNA-seq TruSeq-straded mRNA type. Libraries were sequenced by the Illumina HiSeq 2500 platform (Illumina) as 50bp single reads. Unaligned reads were mapped to the mm10 reference genome using STAR v2.5.3a at default settings. For each condition, total MeRIP reads per transcript were calculated for reads that fully overlapped with a given feature, and were normalized to total non-IP reads per corresponding transcript. This ratio was normalized to corresponding Sham values, and was defined as fold change (FC). Differential peak analysis of m6A MeRIP-Seq datasets were carried out using a modification of exomePeak R/Bioconductor package to compare the ratio of the absolute number of MeRIP reads to non-IP

reads at a given peak between two conditions. To remove false positive signaling in our differential methylation analysis, we have used the same input read threshold as recommended[21]. In other words, differential methylation between two conditions at a given peak was calculated as:

$FC = (Bound_1/non\text{-}IP_1)/(Bound_2/non\text{-}IP_2)$

where FC denotes fold change; $Bound_1$ and $Bound_2$ are the number of reads within a peak for the MeRIP samples for conditions 1 and 2, respectively; and $non\text{-}IP_1$ and $non\text{-}IP_2$ are the number of reads within a peak for the non-IP samples for conditions 1 and 2, respectively. In our differential methylation analysis, fold changes of ±2 between two conditions at a given peak and a formal test with proper FDR (false discovery rate) control (FDR<0.05) were included and considered significant. The data have been deposited in the GEO repository with the accession number GSE112789. MeRIP tracks were visualized with Integrative Genomics Viewer (IGV), using filtered (see above for filtering methods) .bam files from each group at select loci.

For MeRIP-qPCR, immunopurified RNA was purified and first strand cDNA synthesis was carried out as described earlier. Enrichment of mRNA in m6A-immunopurified samples was expressed relative to 18s rRNA in bound samples and expressed as fold change between groups. Taqman primers were used for testing m6A enrichment within transcripts; for RYR2 (Hs00181461_m1), ATP2A2/SERCA2A (Hs00544877_m1).

The DAVID bioinformatics database was used for gene ontology (GO) analysis on significant differentially methylated MeRIP peaks (defined above). GO classification was performed at default settings.

Statistical methods

Data are shown as mean +/- SEM unless otherwise stated. One-way analysis of variance

(ANOVA) was used to determine statistical significance for experiments with more than two groups followed by Bonferroni's post hoc tests. Figures with ANOVA analysis where applicable are indicated in corresponding figure legends. Comparison between two groups were carried out using GraphPad software with an unpaired Student's t-test. P-values <0.05 were considered statistically significant and assigned in individual figures.

Results

Increased m6A in RNA in human, pig and mouse failing hearts

We quantified m6A levels in RNA extracted from failing human (both ischemic and non-ischemic), pig and mouse (post-myocardial infarction ischemic) hearts and compared them to m6A in non-failing human and sham surgical controls respectively. We detected significantly elevated levels of m6A in both total and polyA$^+$ RNA extracted from human, pig and mouse failing left ventricular (LV) explants compared to non-failing or sham (Figure 1A-C). The increase in m6A in total RNA was observed as early as one-week post-MI in mice (Figure 1C) and two weeks post-MI in pigs (Figure 1B). We also observed a sustained increase in m6A in both total and polyA$^+$ RNA in chronic phases of MI-induced heart failure in both mouse and pig ischemic LVs measured at four weeks and twenty weeks respectively (Figure 1B and 1C). Interestingly, the increase in m6A appeared to be confined only to the infarct and peri-infarct regions, as it was not detected in the non-infarct (remote) LV tissues in both pigs and mice in all time points investigated (Figure 1D and 1E). These results provide strong evidence of increases in m6A in RNA in chronic heart failure conditions in humans, which were conserved across species in swine and mouse.

Decreased FTO expression in human and mouse failing hearts

To identify regulators of elevated m6A in failing hearts, we measured expression levels of several known RNAs and proteins associated with m6A methylation (writers, such as METTL3, METTL4 and METTL14 and their regulatory subunit, WTAP) and demethylation (erasers, such as FTO and ALKBH5) [5] in human and mouse hearts. Western blot and qRT-PCR data revealed that expression of FTO (for human; for mouse/rat: Fto) was significantly decreased in failing LV explants from human and mouse, both at the RNA and the protein levels as compared to their respective controls (Figure 2A-2F). The post-ischemic decrease of Fto was detected as early as four hours post-MI in mice hearts and the decrease in Fto mRNA and protein levels consistently correlated with increased m6A at one week and four weeks post-MI in mouse (Figure 2D-2F). Moreover, the transient, inconsistent increase or decrease of other m6A writers and erasers (Figure 2G and Supplemental Figure 1A-1D) could not fully explain the aberrant and sustained increase in m6A in the failing hearts. Interestingly, among all the m6A writers and erasers studied, FTO had the highest baseline expression both at the RNA and protein levels in healthy human (Figure 2A and Supplemental Figure 2A-2B) and no-surgery mouse (Supplemental Figure 2C-2E) LV tissues. Collectively, these data established that ischemia-induced loss of FTO could be an important molecular hallmark that may explain the increase in m6A in human and mouse failing hearts.

Fto-dependent m6A demethylation regulates intracellular Ca^{2+} and sarcomere dynamics in cardiomyocytes

To investigate the role of Fto in cardiomyocytes and to determine if Fto is a direct regulator of m6A, we established cell culture models with loss of Fto using siRNA to *Fto* (siFto) and gain of *Fto* using adenovirus carrying *Fto* (adFto) in isolated adult rat primary cardiomyocytes and compared to siCtrl and adnull controls, respectively (Figure 3A and Supplemental Figure 3A-3B).

Interestingly, expression of *Fto* inversely correlated with the level of m6A in total RNA in primary myocytes (Figure 3A and 3B). Similar to ischemic mouse and human hearts, primary cardiomyocytes subjected to hypoxia had decreased *Fto* expression (Figure 3A) and increased m6A in RNA (Figure 3B). Overexpressing *Fto* in cardiomyocytes cultured under hypoxia reversed the hypoxia-induced aberrant increase in m6A in RNA (Figure 3B) suggesting that Fto is a key regulator of m6A in cardiomyocytes. On the other hand, m6A and Fto levels in adult rat primary non-myocytes subjected to hypoxia remained unchanged compared to normoxic non-myocytes (Supplemental Figure 3C and 3D) suggesting that myocytes are more responsive to Fto-dependent m6A dysregulation than non-myocytes. In the same line, we found that primary cardiomyocytes isolated from healthy human LV has significantly higher expression of FTO compared to primary non-myocytes from the same hearts (Supplemental Figure 4). In addition, human ventricular myocyte cell line, but not human cardiac fibroblasts or endothelial cells in culture had significantly lower FTO mRNA expression under hypoxia stress (Supplemental Figure 4). Together, these data indicate that myocytes regulate FTO expression under hypoxic stress.

To investigate the functional significance of Fto-modulated m6A in cardiomyocyte contractile function in vitro, we measured pacing-induced calcium (Ca^{2+}) dynamics and contractile properties in Fto-modulated primary cardiomyocytes cultured under normoxic and hypoxic conditions. Remarkably, siFto treated myocytes with higher m6A levels exhibited significantly increased number of arrhythmic events as compared to siCtrl cardiomyocytes (Figure 3C and 3D), supporting an earlier observation that a decrease in Fto-demethylase activity leads to proarrhythmic remodeling and altered ventricular repolarization in Fto-deficient mice hearts[16]. On the other hand, hypoxia-induced cardiomyocyte dysfunction was significantly improved by overexpressing Fto in hypoxic cardiomyocytes which resulted in improved Ca^{2+}

amplitude (Figure 3E, and Supplemental Figure 5A), accelerated Ca^{2+} decay (Figure 3F, 3G and Supplemental Figure 5B), increased sarcomere shortening (Figure 3H) and maximum and minimum shortening velocities (Supplemental Figure 5C and 5D) as compared to adnull treated cardiomyocytes. Collectively, these data demonstrate that Fto attenuated hypoxia-induced cardiomyocyte dysfunction in vitro.

Myocardial Fto gene transfer attenuates ischemia-induced loss of cardiac function in mouse failing hearts

To investigate the beneficial function of Fto during cardiac remodeling in vivo, we overexpressed Fto using AAV9 (aavFto) for sustained Fto overexpression pre-MI (Figure 4A, 4B and Supplemental Figure 6A-6C) or using adenovirus (adFto) for transient overexpression post-MI (Figure 5A and 5B) and compared them with the control ischemic (aavgnp-MI or adnull-MI) hearts. Both AAV- and adeno-mediated overexpression of Fto significantly decreased the MI-induced increase of m6A in RNA (Figure 4C and 5C and Supplemental Figure 6D) but did not affect the expression of other m6A writers and erasers (Supplemental Figures 6E-6G, 7A-7D and 8A-8D). Body weight measurements throughout the study period indicated no significant changes between control and Fto overexpressing mice (Supplemental Figure 9A-D) suggesting that either sustained or transient overexpression of FTO in the myocardium may not have direct effect on body weight. Interestingly, Fto overexpression significantly improved cardiac function at the chronic stages of post-MI as indicated by higher ejection fraction (Figure 4D and 5D, Supplemental Figure 10A, 10D and 10G), fractional shortening (Figure 4E and 5E, Supplemental Figure 10B, 10E and 10G)and improved wall motion (Figure 4F and 5F, Supplemental Figure 10C and 10F) both at two and four weeks post-MI. To address the functional mechanisms of FTO-induced cardiac repair, we quantified fibrosis and angiogenesis in FTO overexpressing

(AAV or adenovirus) mice and compared them to AAV/adenonull mice post-MI. Interestingly, fibrosis, as determined by scar size (%), was significantly reduced in FTO overexpressing (aavFto-MI or adFto-MI) mice compared to respective controls (aavgnp-MI or adnull-MI) quantified at four weeks (Figure 4G, 4H and 5G, 5H). Similarly we determined angiogenic response by quantifying CD31-positive endothelial cells in the murine hearts at the infarct border zone at four weeks post-MI. Both aavFto and adFto overexpressing hearts had significantly higher number of CD31-positive cells compared to aavgnp and adnull control hearts (Supplemental Figure 11). These data suggest that both sustained and transient overexpression of Fto resulting in lower m6A is beneficial for the heart and can improve MI-induced cardiac dysfunction. Moreover, transient overexpression of Fto starting after few days of adenovirus injection post-MI significantly improved cardiac function suggesting potential therapeutic application of FTO or FTO mimics in the treatment of heart failure.

Contractile transcripts hypermethylated in failing hearts are demethylated by Fto overexpression

To identify the m6A demethylating targets of Fto in the transcriptome, we performed immunoprecipitation of m6A-modified RNA (MeRIP) followed by sequencing from sham, MI, aavgnp-MI and aavFto-MI mouse LV tissues from peri-infarct area (Supplemental Figure12) [4, 22]. Differential expression of individual transcripts across conditions can affect perceived m6A enrichment in MeRIP; therefore, to identify differential m6A modifications across conditions independent of varying transcription [4, 21], we normalized MeRIP reads to corresponding non-IP reads within each condition using a modified ExomePeak analysis (Supplemental Figure12).

Transcriptome-wide methylation represented by total number of MeRIP reads indicated global hypermethylation in MI compared to sham (Figure 6A). These data are consistent with our earlier observation of increase in m6A in failing LVs in vivo (Figure 1A-1C) and in adult primary myocytes under hypoxia in vitro (Figure 3B). While this hypermethylation effect was also evident in aavgnp-MI, overexpression of Fto (aavFto-MI) led to apparent global demethylation (Figure 6A). Analysis of total MeRIP reads (normalized to non-IP reads) for each transcript in sham, MI, aavgnp-MI and aavFto-MI suggests overexpressing Fto in MI hearts reversed the MI-induced global hypermethylation as aavFto-MI clustered with sham (Supplemental Figure13A). It also suggests that Fto demethylates a subset of transcripts (Figure 6B) that are largely associated with cardiac hypertrophy, muscle contraction, filament sliding and sarcomere organization (Figure 6C and Supplemental Tables S1-S8). MeRIP-seq map of individual transcripts show hypermethylated sites in MI compared to sham for several Ca^{2+} and contractile transcripts such as *Nppa, Myh7, Serca2a, Ryr2*, as well as myocardium-specific lncRNAs *Mhrt* and *Chast*, which were demethylated in aavFto-MI (Figure 6D and Supplemental Tables S3 and S4). In addition, our MeRIP-seq identified that FTO overexpression resulted in regulation of angiogenic and fibrotic (ECM) pathways (Supplemental Tables S4 and S8). Our results confirm prior observations of *Serca2a* methylation in 3T3L1 pre-adipocytes and in HeLa cells in response to heat shock [23-25]. PCR analyses of MeRIP enriched RNA from human LV tissues confirmed that Ca^{+2} handling transcripts *SERCA2a*, and *RYR2* were hypermethylated in the failing human hearts (Figure 7A). Consistent with this, *SERCA2a* mRNA was demethylated when Fto was overexpressed in human myocytes (Figure 7B and Supplemental Figure13B and 13C) resulting in increased *SERCA2a* mRNA expression (Figure 7C). Indeed, these effects were translated to mouse post-MI in FTO overexpressing LV tissues (Figure 7D and Figure 7E).

Demethylation of *SERCA2a* mRNA and its association with increased mRNA levels could be a result of FTO increasing the stability of *SERCA2a* mRNA and possibly of other contractile mRNAs [26, 27] or a co-transcriptional regulation by FTO [19]. Our in vivo data showing increased Serca2a protein expression in aavFto-MI and adFto-MI mice corroborated our findings (Figure 7F). Collectively, our MeRIP analysis confirmed transcriptome-wide hypermethylation post-MI, demethylation with Fto gene delivery and Fto targeting a subset of mRNAs involved in positive regulation of calcium and contractile function during cardiac remodeling.

Our results have uncovered dysregulation of m6A as an important molecular hallmark of post-ischemic cardiac remodeling and a novel layer of gene regulation at the RNA level in heart failure.

Discussion

In this study, we have found compelling in vitro, in vivo and translational evidence demonstrating an important role for FTO in cardiomyocyte and cardiac function under physiological, pathological and reparative conditions. We have identified FTO as a key myocardial demethylase that regulates cardiac m6A and provided a novel characterization of FTO-dependent m6A in cardiac contractile function. FTO expression is downregulated in heart failure, leading to aberrant increase in global cardiac m6A as well as m6A in selective contractile transcripts leading to their decreased protein expression. Loss of FTO resulted in anomalous calcium handling and sarcomere dynamics resulting in loss of contractile function in primary cardiomyocytes. Interestingly, forced expression of FTO in stressed hypoxic cardiomyocytes or failing murine myocardium attenuated ischemia-induced cardiac remodeling, loss of cardiac contractile protein expression and loss of cardiac contractile function, demonstrating therapeutic

potential of FTO. By comparing the cardiac m6A maps of individual transcripts we discovered that FTO selectively demethylates cardiac contractile transcripts such as *SERCA2A*, *MYH6*/7, *RYR2* and many others improving their mRNA and protein expression. We have further shown that the cardioprotective mechanism of FTO is mediated by selective demethylation of cardiac contractile transcripts under ischemia, which increases mRNA stability and protein expression[10, 28, 29]. Our MeRIP-seq pathway analysis indicate that FTO acts on selective cardiac pathways such as those relevant to sarcomere organization, myofibril assembly, calcium handling and contractility (Figure 6C, Tables S3, S4, S7 and S8). In addition, it also acts on pathways related to angiogenesis and fibrosis (ECM) and on lncRNAs including *Chast* or Mhrt, which are implicated in fibrosis and hypertrophy (Figure 6D, Tables S4 and S8). In addition to restoring contractile protein expression such as SERCA2A, we provided experimental evidence that FTO overexpression decreased cardiac fibrosis and enhanced angiogenesis in the ischemic myocardium. Our study demonstrates functional importance of FTO-dependent cardiac m6A methylome in cardiac contraction, fibrosis and angiogenesis during heart failure and provides robust mechanistic insights into the therapeutic potential of FTO (Figure 8).

FTO is a dioxygenase that oxidatively demethylates m6A-containing mRNAs [12]. Thus, the enzymatic activity of FTO may be expected to decrease under hypoxic or ischemic conditions independent of its expression levels. Interestingly, we also found that both hypoxia in primary cardiomyocytes and ischemia in mouse hearts have reduced expression of FTO, both at the protein and the RNA level. There could be several direct and indirect mechanisms for FTO downregulation under hypoxic/ischemic stress, including hypoxia-inducible miRNA binding. We identified binding sites in *FTO* mRNA for several hypoxia inducible cardiac miRs such as miR-21, miR-24, miR-488, miR-224, miR-489 and miR-199:miR-214 cluster[30, 31], (many of) which

are known to be upregulated in heart failure. A direct role for these miRs could reveal upstream pathways of FTO regulation in heart failure. Both transcriptional and post-transcriptional suppression of FTO as well as hypoxia-induced reduction in FTO activity support our in vitro and in vivo observations of increase in m6A upon FTO silencing, in hypoxia and in heart failure.

By modulating FTO expression through silencing or overexpression in isolated primary cardiac myocytes, we have demonstrated that FTO is a key contributor of global m6A levels. Further, FTO expression inversely correlates with m6A and FTO-dependent m6A is a novel and positive regulator of cardiomyocyte and cardiac contractile function. In this line, a recent study investigated FTO in myoblast differentiation and found that FTO depletion interfered with myogenic differentiation highlighting that FTO is required for myogenesis [28]. These data implicate FTO as an important regulator of muscle physiology.

As m6A demethylation in a single stranded nuclear RNA is the only known primary function of FTO, we attribute the effects of FTO alteration directly to changes in m6A in the target transcripts. Nevertheless, we do not rule out FTO-dependent N^6,2'-O-dimethyladenosine ($m6A_m$) demethylation [32], long noncoding RNA demethylation or other indirect effects resulting from FTO (m6A)-regulated transcriptional co-regulatory networks or miRNA expression. Moreover, in addition to FTO downregulation, we detected elevated levels of writer proteins such as METTL4/14 in human and Mettl14 in mouse failing hearts, suggesting that these writers possibly also contribute to the increased m6A in failing hearts. Whether these writers compete with FTO to target similar subsets and locations of transcripts or function in a mutually exclusive manner needs to be investigated. Interestingly, the increase in transcriptome-wide m6A was significant only at one-week post-MI although FTO expression was downregulated as early as four hours post-MI. This discrepancy in transcriptome-wide m6A increase could be explained by

the upregulation of another closely relatedm6A demethylase, ALKBH5, at four hours and one-day post-MI. An increase in ALKBH5 could offset the increased m6A resulting from loss of FTO at both four hours and one-day time points. This claim was corroborated by the observation that ALKBH5 protein expression returned to normal levels comparable to control hearts at one week and four-week post-MI, effectively increasing global m6A levels at those time points-primarily resulting from loss of FTO and partially from the transient increase in m6A writers. As m6A is dynamically regulated, the interplay between writer, eraser and reader proteins could be important regulating the protein expression during cardiac remodeling and regeneration, and therefore, needs to be determined.

Transcriptome-wide m6A profiling of failing mouse hearts indicated hypermethylation of several transcripts encoding cardiac contractile proteins. Previous studies have shown that hypermethylated transcripts are less stable and negatively regulate translation [6, 33, 34]. Consistently, we detected hypermethylation in contractile transcripts including *MYH6*, *RYR2*, *SERCA2a* etc., whose expressions are known to be significantly decreased in human and mouse failing hearts. This finding corroborated our in vitro data with FTO depletion or hypoxic treatment increased the m6A that resulted in aberrant cardiomyocyte calcium handling and contractile function. On the other hand, forced expression of FTO in mouse failing hearts resulted in demethylation of contractile transcripts (*SERCA2a*), bringing their m6A to near normal level. This resulted in significant improvement in contractile protein (*SERCA2a*) expression and cardiac function as demonstrated by improved ejection fraction and fractional shortening. Our observation of positive regulation of contractile transcripts and proteins with FTO-dependent demethylation are consistent with previous observations, where m6A

demethylation by FTO has been shown to promote mRNA and protein expression including expression of myosin heavy chain proteins [10, 28, 29].

In addition to positively regulating contractile protein expression, Fto-dependent demethylation could also regulate non-contractile protein expression in cardiomyocytes, in line with a recent study reporting that FTO-dependent m6A demethylation negatively regulated mRNA and protein expression in AML cancer cells [9]. In our study, we did not find any significant effect of hypoxia on FTO expression and on global m6A levels in non-myocytes in vitro. However, we cannot not rule out altered m6A sites within individual transcripts under hypoxia that may have functional roles. Interestingly, our MeRIP sequencing analysis revealed that in addition to contractile pathways, FTO-overexpression regulates important non-contractile pathways as well, including tissue morphogenesis, angiogenesis, extracellular matrix organization, fibrosis, and cell growth in murine MI hearts. These MeRIP data was supported by experimental observations of enhanced angiogenesis as well as reduced scar size in the FTO-overexpressed murine MI hearts. Collectively, these data suggest that FTO-dependent m6A regulates both contractile and non-contractile pathways in murine myocardium. Whether these non-contractile phenotypes are direct functional effects of m6A on non-contractile transcripts and pathways or indirect effects of m6A-dependent transcripts and pathways needs further investigation.

Our analysis of hypermethylated transcripts in failing hearts revealed pathways involving heart rate and muscle contraction, which have decreased expression at the mRNA and proteins level in failing hearts. Interestingly, our MeRIP analysis also detected several transcripts whose m6A levels were not affected by myocardial infarction surgery or by FTO overexpression, whereas, their protein expressions are known to be differentially regulated in failing mouse and

human hearts. This observation possibly indicates site-specific demethylation of the transcript that is not reflected in the overall m6A quantification, downstream regulation of mRNA transport and processing by FTO or additional unknown mechanisms of FTO function [35]. Increased or decreased expression of proteins as a result of FTO-dependent mRNA demethylation could be regulated by mRNA stability [19, 24], degradation [6], and the rate of translation [26]. In fact, m6A has been shown to have both stimulatory [24, 26] and inhibitory [19, 36] effects on the translation dynamics. The precise effect of m6A on translation may depend on the specific 5' and 3' location of m6A within the transcript [19, 24, 37]. The site-specific m6A maps of transcripts, and its role in translation warrants further investigation.

m6A has been shown to regulate stem cell renewal [38], however a direct evidence for m6A in tissue regeneration and repair has not been established. Here, we identified a novel role for m6A and myocardial m6A demethylase, FTO, in regulating cardiac tissue repair and contractile function after myocardial ischemia. In addition to the sustained expression of FTO using AAV9 vector, we detected significant beneficial effects of transiently expressed FTO delivered post-ischemia using adFTO. This indicates that FTO is therapeutic and FTO-mediated m6A demethylation can induce homeostatic protein expression resulting in improved cardiac function. It is notable that Fto levels were downregulated as early as 4 hours post-MI in mouse. Adenovirus mediated gene delivery, which maximizes FTO expression in 2 days and provides stable FTO expression for about a week, could improve cardiac homeostasis and function following the initial remodeling phase induced by MI. This transient FTO overexpression following initial remodeling phase as well as sustained FTO overexpression using AAV9 suggest that FTO-mediated benefits could be a result of both protective and reparative mechanisms of FTO. However, further studies are warranted to specifically address the precise mechanisms of

FTO-mediated beneficial action. This data strongly suggests a potential therapeutic application of FTO in the treatment of post-ischemic heart failure. Fto or FTO mimics can be an interesting next generation therapeutics that can target and simultaneously improve the expression of several key contractile proteins in the heart.

Furthermore, there is an ongoing debate for a role of FTO in obesity and body weight with several studies reporting either positive or negative association for FTO with body mass [39, 40]. We did not observe significant differences in body weights between the control and FTO-overexpressing mice. While we show cardioprotective function of FTO, a better understanding of effect of FTO in body mass is required to take advantage of its clinical potential for the treatment of human heart failure. Together, our data provides proof of principle that given the functional importance of FTO in cardiac homeostasis and myocardial repair, targeting FTO signaling may represent a promising therapeutic strategy to treat heart failure. Our findings on the dynamic nature of the cardiac m6A-epitranscriptome will lead to deeper understanding of the mechanism of cardiac remodeling on one hand and innovative therapeutic interventions on the other.

Acknowledgments

We would like to acknowledge the National Disease Research Interchange (NDRI) for providing human LV tissues, Jaegyun Oh from the Icahn School of Medicine, Mount Sinai, New York, for assistance with cardiomyocyte experiments and Ivan Lukic from PartekInc for assistance with bioinformatics analysis to MeRIP-Seq datasets. We also thank Gene Therapy Resource Program (GTRP) of the National Heart, Lung and Blood Institute, National Institutes of Health for providing the gene vectors used in this study.

Sources of Funding

This work was supported by grants from National Institute of Health (NIH) HL124187, HL140469, American Heart Association (AHA) 17GRNT33460554 to SS, and AHA postdoctoral grants 17POST33670354 to PM and 17POST33410648 to YL, NIH HL117505, HL119046, HL129814, HL128072, HL131404, HL135093 and a Transatlantic Foundation Leducq grant to RJH, NH HL137220, HL097357 and G050071 grants to DL, AHA 17SDG33410873 to KI and AHA 17SDG33370112 to YS.

Disclosures

None

References

1. Su YR, Chiusa M, Brittain E, Hemnes AR, Absi TS, Lim CC and Di Salvo TG. Right ventricular protein expression profile in end-stage heart failure. *Pulm Circ*. 2015;5:481-97.
2. Brundel BJ, Van Gelder IC, Henning RH, Tuinenburg AE, Wietses M, Grandjean JG, Wilde AA, Van Gilst WH and Crijns HJ. Alterations in potassium channel gene expression in atria of patients with persistent and paroxysmal atrial fibrillation: differential regulation of protein and mRNA levels for K+ channels. *J Am Coll Cardiol*. 2001;37:926-32.
3. Preissl S, Schwaderer M, Raulf A, Hesse M, Gruning BA, Kobele C, Backofen R, Fleischmann BK, Hein L and Gilsbach R. Deciphering the Epigenetic Code of Cardiac Myocyte Transcription. *Circ Res*. 2015;117:413-23.
4. Meyer KD, Saletore Y, Zumbo P, Elemento O, Mason CE and Jaffrey SR. Comprehensive analysis of mRNA methylation reveals enrichment in 3' UTRs and near stop codons. *Cell*. 2012;149:1635-46.
5. Fu Y, Dominissini D, Rechavi G and He C. Gene expression regulation mediated through reversible m(6)A RNA methylation. *Nat Rev Genet*. 2014;15:293-306.
6. Wang X, Lu Z, Gomez A, Hon GC, Yue Y, Han D, Fu Y, Parisien M, Dai Q, Jia G, Ren B, Pan T and He C. N6-methyladenosine-dependent regulation of messenger RNA stability. *Nature*. 2014;505:117-20.
7. Liu N, Zhou KI, Parisien M, Dai Q, Diatchenko L and Pan T. N6-methyladenosine alters RNA structure to regulate binding of a low-complexity protein. *Nucleic Acids Res*. 2017;45:6051-6063.
8. Zhang S, Zhao BS, Zhou A, Lin K, Zheng S, Lu Z, Chen Y, Sulman EP, Xie K, Bogler O, Majumder S, He C and Huang S. m6A Demethylase ALKBH5 Maintains Tumorigenicity of

Glioblastoma Stem-like Cells by Sustaining FOXM1 Expression and Cell Proliferation Program. *Cancer Cell*. 2017;31:591-606 e6.
9. Li Z, Weng H, Su R, Weng X, Zuo Z, Li C, Huang H, Nachtergaele S, Dong L, Hu C, Qin X, Tang L, Wang Y, Hong GM, Huang H, Wang X, Chen P, Gurbuxani S, Arnovitz S, Li Y, Li S, Strong J, Neilly MB, Larson RA, Jiang X, Zhang P, Jin J, He C and Chen J. FTO Plays an Oncogenic Role in Acute Myeloid Leukemia as a N(6)-Methyladenosine RNA Demethylase. *Cancer Cell*. 2017;31:127-141.
10. Hess ME, Hess S, Meyer KD, Verhagen LA, Koch L, Bronneke HS, Dietrich MO, Jordan SD, Saletore Y, Elemento O, Belgardt BF, Franz T, Horvath TL, Ruther U, Jaffrey SR, Kloppenburg P and Bruning JC. The fat mass and obesity associated gene (Fto) regulates activity of the dopaminergic midbrain circuitry. *Nat Neurosci*. 2013;16:1042-8.
11. Zhao BS, Roundtree IA and He C. Post-transcriptional gene regulation by mRNA modifications. *Nat Rev Mol Cell Biol*. 2017;18:31-42.
12. Jia G, Fu Y, Zhao X, Dai Q, Zheng G, Yang Y, Yi C, Lindahl T, Pan T, Yang YG and He C. N6-methyladenosine in nuclear RNA is a major substrate of the obesity-associated FTO. *Nature chemical biology*. 2011;7:885-7.
13. Church C, Moir L, McMurray F, Girard C, Banks GT, Teboul L, Wells S, Bruning JC, Nolan PM, Ashcroft FM and Cox RD. Overexpression of Fto leads to increased food intake and results in obesity. *Nat Genet*. 2010;42:1086-92.
14. Shen F, Huang W, Huang JT, Xiong J, Yang Y, Wu K, Jia GF, Chen J, Feng YQ, Yuan BF and Liu SM. Decreased N(6)-methyladenosine in peripheral blood RNA from diabetic patients is associated with FTO expression rather than ALKBH5. *J Clin Endocrinol Metab*. 2015;100:E148-54.
15. Boissel S, Reish O, Proulx K, Kawagoe-Takaki H, Sedgwick B, Yeo GS, Meyre D, Golzio C, Molinari F, Kadhom N, Etchevers HC, Saudek V, Farooqi IS, Froguel P, Lindahl T, O'Rahilly S, Munnich A and Colleaux L. Loss-of-function mutation in the dioxygenase-encoding FTO gene causes severe growth retardation and multiple malformations. *Am J Hum Genet*. 2009;85:106-11.
16. Carnevali L, Graiani G, Rossi S, Al Banchaabouchi M, Macchi E, Quaini F, Rosenthal N and Sgoifo A. Signs of cardiac autonomic imbalance and proarrhythmic remodeling in FTO deficient mice. *PLoS One*. 2014;9:e95499.
17. Gustavsson J, Mehlig K, Leander K, Lissner L, Bjorck L, Rosengren A and Nyberg F. FTO genotype, physical activity, and coronary heart disease risk in Swedish men and women. *Circ Cardiovasc Genet*. 2014;7:171-7.
18. Zhang C, Samanta D, Lu H, Bullen JW, Zhang H, Chen I, He X and Semenza GL. Hypoxia induces the breast cancer stem cell phenotype by HIF-dependent and ALKBH5-mediated m6A-demethylation of NANOG mRNA. *Proc Natl Acad Sci U S A*. 2016.
19. Slobodin B, Han R, Calderone V, Vrielink JA, Loayza-Puch F, Elkon R and Agami R. Transcription Impacts the Efficiency of mRNA Translation via Co-transcriptional N6-adenosine Methylation. *Cell*. 2017;169:326-337 e12.
20. Barbieri I, Tzelepis K, Pandolfini L, Shi J, Millan-Zambrano G, Robson SC, Aspris D, Migliori V, Bannister AJ, Han N, De Braekeleer E, Ponstingl H, Hendrick A, Vakoc CR, Vassiliou GS and Kouzarides T. Promoter-bound METTL3 maintains myeloid leukaemia by m(6)A-dependent translation control. *Nature*. 2017;552:126-131.

21. Meng J, Lu Z, Liu H, Zhang L, Zhang S, Chen Y, Rao MK and Huang Y. A protocol for RNA methylation differential analysis with MeRIP-Seq data and exomePeak R/Bioconductor package. *Methods*. 2014;69:274-81.
22. Dominissini D, Moshitch-Moshkovitz S, Schwartz S, Salmon-Divon M, Ungar L, Osenberg S, Cesarkas K, Jacob-Hirsch J, Amariglio N, Kupiec M, Sorek R and Rechavi G. Topology of the human and mouse m6A RNA methylomes revealed by m6A-seq. *Nature*. 2012;485:201-6.
23. Zhao X, Yang Y, Sun BF, Shi Y, Yang X, Xiao W, Hao YJ, Ping XL, Chen YS, Wang WJ, Jin KX, Wang X, Huang CM, Fu Y, Ge XM, Song SH, Jeong HS, Yanagisawa H, Niu Y, Jia GF, Wu W, Tong WM, Okamoto A, He C, Rendtlew Danielsen JM, Wang XJ and Yang YG. FTO-dependent demethylation of N6-methyladenosine regulates mRNA splicing and is required for adipogenesis. *Cell Res*. 2014;24:1403-19.
24. Meyer KD, Patil DP, Zhou J, Zinoviev A, Skabkin MA, Elemento O, Pestova TV, Qian SB and Jaffrey SR. 5' UTR m(6)A Promotes Cap-Independent Translation. *Cell*. 2015;163:999-1010.
25. Zhou J, Wan J, Gao X, Zhang X, Jaffrey SR and Qian SB. Dynamic m(6)A mRNA methylation directs translational control of heat shock response. *Nature*. 2015;526:591-4.
26. Wang X, Zhao BS, Roundtree IA, Lu Z, Han D, Ma H, Weng X, Chen K, Shi H and He C. N(6)-methyladenosine Modulates Messenger RNA Translation Efficiency. *Cell*. 2015;161:1388-99.
27. Wang Y, Li Y, Toth JI, Petroski MD, Zhang Z and Zhao JC. N6-methyladenosine modification destabilizes developmental regulators in embryonic stem cells. *Nat Cell Biol*. 2014;16:191-8.
28. Wang X, Huang N, Yang M, Wei D, Tai H, Han X, Gong H, Zhou J, Qin J, Wei X, Chen H, Fang T and Xiao H. FTO is required for myogenesis by positively regulating mTOR-PGC-1alpha pathway-mediated mitochondria biogenesis. *Cell Death Dis*. 2017;8:e2702.
29. Su R, Dong L, Li C, Nachtergaele S, Wunderlich M, Qing Y, Deng X, Wang Y, Weng X, Hu C, Yu M, Skibbe J, Dai Q, Zou D, Wu T, Yu K, Weng H, Huang H, Ferchen K, Qin X, Zhang B, Qi J, Sasaki AT, Plas DR, Bradner JE, Wei M, Marcucci G, Jiang X, Mulloy JC, Jin J, He C and Chen J. R-2HG Exhibits Anti-tumor Activity by Targeting FTO/m(6)A/MYC/CEBPA Signaling. *Cell*. 2017.
30. el Azzouzi H, Leptidis S, Dirkx E, Hoeks J, van Bree B, Brand K, McClellan EA, Poels E, Sluimer JC, van den Hoogenhof MM, Armand AS, Yin X, Langley S, Bourajjaj M, Olieslagers S, Krishnan J, Vooijs M, Kurihara H, Stubbs A, Pinto YM, Krek W, Mayr M, da Costa Martins PA, Schrauwen P and De Windt LJ. The hypoxia-inducible microRNA cluster miR-199a approximately 214 targets myocardial PPARdelta and impairs mitochondrial fatty acid oxidation. *Cell Metab*. 2013;18:341-54.
31. Kulshreshtha R, Ferracin M, Wojcik SE, Garzon R, Alder H, Agosto-Perez FJ, Davuluri R, Liu CG, Croce CM, Negrini M, Calin GA and Ivan M. A microRNA signature of hypoxia. *Mol Cell Biol*. 2007;27:1859-67.
32. Mauer J, Luo X, Blanjoie A, Jiao X, Grozhik AV, Patil DP, Linder B, Pickering BF, Vasseur JJ, Chen Q, Gross SS, Elemento O, Debart F, Kiledjian M and Jaffrey SR. Reversible methylation of m(6)Am in the 5' cap controls mRNA stability. *Nature*. 2017;541:371-375.
33. Schwartz S, Mumbach MR, Jovanovic M, Wang T, Maciag K, Bushkin GG, Mertins P, Ter-Ovanesyan D, Habib N, Cacchiarelli D, Sanjana NE, Freinkman E, Pacold ME, Satija R, Mikkelsen TS, Hacohen N, Zhang F, Carr SA, Lander ES and Regev A. Perturbation of m6A

writers reveals two distinct classes of mRNA methylation at internal and 5' sites. *Cell Rep*. 2014;8:284-96.
34. Zhao BS, Wang X, Beadell AV, Lu Z, Shi H, Kuuspalu A, Ho RK and He C. m6A-dependent maternal mRNA clearance facilitates zebrafish maternal-to-zygotic transition. *Nature*. 2017.
35. Xiang Y, Laurent B, Hsu CH, Nachtergaele S, Lu Z, Sheng W, Xu C, Chen H, Ouyang J, Wang S, Ling D, Hsu PH, Zou L, Jambhekar A, He C and Shi Y. RNA m6A methylation regulates the ultraviolet-induced DNA damage response. *Nature*. 2017;543:573-576.
36. Choi J, Ieong KW, Demirci H, Chen J, Petrov A, Prabhakar A, O'Leary SE, Dominissini D, Rechavi G, Soltis SM, Ehrenberg M and Puglisi JD. N(6)-methyladenosine in mRNA disrupts tRNA selection and translation-elongation dynamics. *Nat Struct Mol Biol*. 2016;23:110-5.
37. Lence T, Akhtar J, Bayer M, Schmid K, Spindler L, Ho CH, Kreim N, Andrade-Navarro MA, Poeck B, Helm M and Roignant JY. m6A modulates neuronal functions and sex determination in Drosophila. *Nature*. 2016;540:242-247.
38. Geula S, Moshitch-Moshkovitz S, Dominissini D, Mansour AA, Kol N, Salmon-Divon M, Hershkovitz V, Peer E, Mor N, Manor YS, Ben-Haim MS, Eyal E, Yunger S, Pinto Y, Jaitin DA, Viukov S, Rais Y, Krupalnik V, Chomsky E, Zerbib M, Maza I, Rechavi Y, Massarwa R, Hanna S, Amit I, Levanon EY, Amariglio N, Stern-Ginossar N, Novershtern N, Rechavi G and Hanna JH. Stem cells. m6A mRNA methylation facilitates resolution of naive pluripotency toward differentiation. *Science*. 2015;347:1002-6.
39. Smemo S, Tena JJ, Kim KH, Gamazon ER, Sakabe NJ, Gomez-Marin C, Aneas I, Credidio FL, Sobreira DR, Wasserman NF, Lee JH, Puviindran V, Tam D, Shen M, Son JE, Vakili NA, Sung HK, Naranjo S, Acemel RD, Manzanares M, Nagy A, Cox NJ, Hui CC, Gomez-Skarmeta JL and Nobrega MA. Obesity-associated variants within FTO form long-range functional connections with IRX3. *Nature*. 2014;507:371-5.
40. Claussnitzer M, Dankel SN, Kim KH, Quon G, Meuleman W, Haugen C, Glunk V, Sousa IS, Beaudry JL, Puviindran V, Abdennur NA, Liu J, Svensson PA, Hsu YH, Drucker DJ, Mellgren G, Hui CC, Hauner H and Kellis M. FTO Obesity Variant Circuitry and Adipocyte Browning in Humans. *N Engl J Med*. 2015;373:895-907.

Figure Legends

Figure 1. Increased m6A in RNA in failing human (both ischemic and non-ischemic), pig and mouse (post-myocardial infarction ischemic) hearts.

Quantification of m6A in total or polyA$^+$ RNA in LV of **A**, human, n=6-11; from infarct/peri-infarct areain **B**, pig, n=3-6, **C**, mouse, n=5-11; from non-infarct area in **D**, pig, n=3 and **E**, mouse, n=3-6. Error bars represent SEM. **P*<0.05, ***P*<0.01, ****P*<0.001, compared with non-failing or sham. n.s., non significant.

Figure 2. Decreased FTO mRNA and protein expression in human and mouse failing hearts.

A,quantification of mRNA, n=3-6, **B**, representative immunoblots, **C**, densitometry quantification of protein, *n*=5-8 for m6A regulators in human non-failing and failing hearts. **D**, quantification of mRNA, n=3-7, **E**, representative immunoblots and **F**, densitometry quantification of protein, *n*=3-4 at different time points in mouse LV. **G**, qRT-PCR quantification of selected mRNA expressions in mouse LV, n=4-8. mRNA/protein data represented as F/MI normalized to NF/sham. Error bars represent SEM. **P*<0.05, ***P*<0.01, ****P*<0.001, compared with non-failing or sham.

Figure 3. Fto-mediated m6A demethylation regulates intracellular Ca^{2+} recycling and contractile dynamics in isolated adult rat primary cardiomyocytes.

Quantification of **A,** Fto mRNA, n=3-4, **B,** m6A in total RNA, n=3-5, **C,** cells with arrhythmic events, n=47-90 cells per group from 4-12 rats. **D,** Representative Ca^{2+} transients obtained from

pacing-induced myocytes. Measurements of **E,** maximal Ca^{2+} amplitude, **F,** time to 50% decay, **G,** Tau, **H,** cell shortening, n=23-74 cells per group from 4-12 rats. Sarcomere and Ca^{2+} transients were recorded at 1Hz pacing stimulation frequency with MyoPacer Field Stimulator (IonOptix MA, USA). Abbreviations, Unt: untreated; siCtrl: siRNA control, siFto: siRNA-mediated Fto knockdown, adnull: adenovirus with empty CMV promoter, adFto: adenovirus with full length Fto. Error bars represent SEM. **P*<0.05, ***P*<0.01, ****P*<0.001by one-way ANOVA.

Figure 4. AAV9-mediated myocardial FTO gene transfer rescues cardiac function in mouse models of MI.

A, Design of aavFto study. **B**, representative immunoblots showing Fto protein expression at week 0 of the aavFto study. **C**, m6A quantification in total RNA at week 4 of aavFto study, n=4-7. Echocardiographic assessments of LV function showing **D,** ejection fraction (EF) and **E,** fractional shortening (FS) at 4w post-MI, n=10-13. **F**, representative M-Mode echocardiograms showing anterior and posterior LV wall motion at 4w post-MI in aavFto mice. Error bars represent SEM. **G,** Representative Masson trichrome staining images of histological cross-sections taken in bright-field mode processed from sham, aavgnp-MI or aavFto-MI. **H,**Scar Size was measured as percentage of total LV area after Masson trichrome staining in sham, aavgnp-MI and aavFto-MI at four weeks post-MI surgeries. Error bars represent SD. **P*<0.05, ****P*<0.001by one-way ANOVA.

Figure 5. Adenovirus-mediated myocardial FTO gene transfer rescues cardiac function in mouse models of MI.

A, Design of adFto study. **B**, representative immunoblots showing Fto protein expression at week 4 of the adFto study. **C**, m6A quantification in total RNA at week 4 of adFto study, n=3-5. Echocardiographic assessments of LV function showing **D,** ejection fraction (EF) and **E,** fractional shortening (FS) at 4w post-MI, n=6-9. **F**, representative M-Mode echocardiograms showing anterior and posterior LV wall motion at 4w post-MI in adFto mice. Error bars represent SEM. **G,** Representative Masson trichrome staining images of histological cross-sections taken in bright-field mode processed from sham, adnull-MI or adFto-MI. **H,**Scar Size was measured as percentage of total LV area after Masson trichrome staining in sham, adnull-MI and adFto-MI at four weeks post-MI surgeries. Error bars represent SD. **P*<0.05, ****P*<0.001 by one-way ANOVA.

Figure 6. Contractile transcripts hypermethylated in failing hearts are demethylated by Fto overexpression.

A, total MeRIP bound reads from mouse MeRIP-Seq. **B,** mouse heatmap showing total MeRIP reads normalized to total non-IP reads within each transcript relative to sham. For each condition, total MeRIP reads per transcript were calculated for reads that fully overlapped with a given feature, and were normalized to total non-IP reads per corresponding transcript. **C,** top 10 DAVID GO terms enriched (±2-fold + FDR<0.05) from mouse MeRIP-Seq. Differential peak analysis of m6A MeRIP-Seq datasets were carried out using a modification of exomePeak R/Bioconductor package to compare the ratio of the absolute number of MeRIP reads to non-IP reads at a given peak between two conditions. **D,** IGV plots of mouse MeRIP reads for selected transcripts, IGV numbers indicate scale for MeRIP reads for all conditions per transcript.

Figure 7. *Serca2a* mRNA is hypermethylated in human failing hearts and demethylation by FTO overexpression induces Serca2a mRNA and protein expression.

A, human MeRIP-qPCR showing m6A enrichment in mRNA. **B,***FTO* mRNA and **C,** *SERCA2A* mRNA, n=3 expressions in AC16 human myocytes. *Fto* mRNA expression in **D,** aavFto-MI and **E**, adFto mice 4w post-MI, n=3-5. **F,** Representative immunoblots showing Serca2a protein expression at 4w post-MI. Error bars represent SEM. **P*<0.05, ****P*<0.001. A-C, student t-test; D and E, one-way ANOVA.

Figure 8. Proposed working model based on our hypothesis.

A, Healthy heart with physiological FTO and m6A levels, **B**, Failing heart with decreased FTO, increased m6A, increased contractile mRNA degradation and dysfunctional myofilament, **C**, Fto rescued failing heart with attenuated m6A and restored contractile protein expression and myofilament.

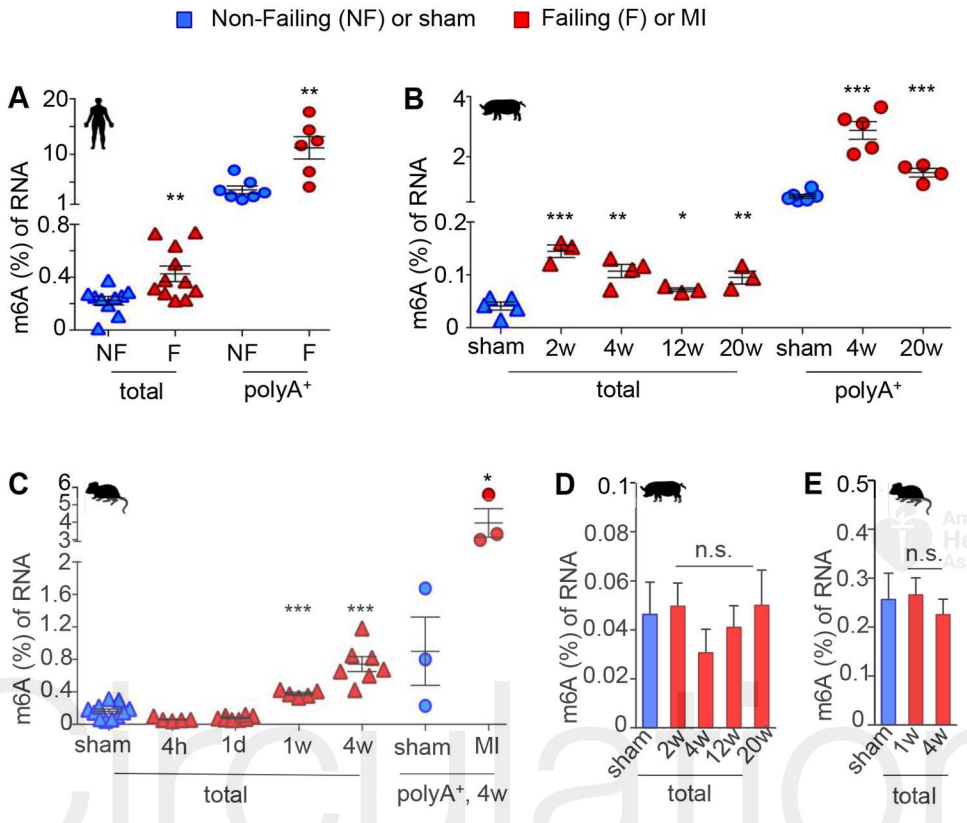

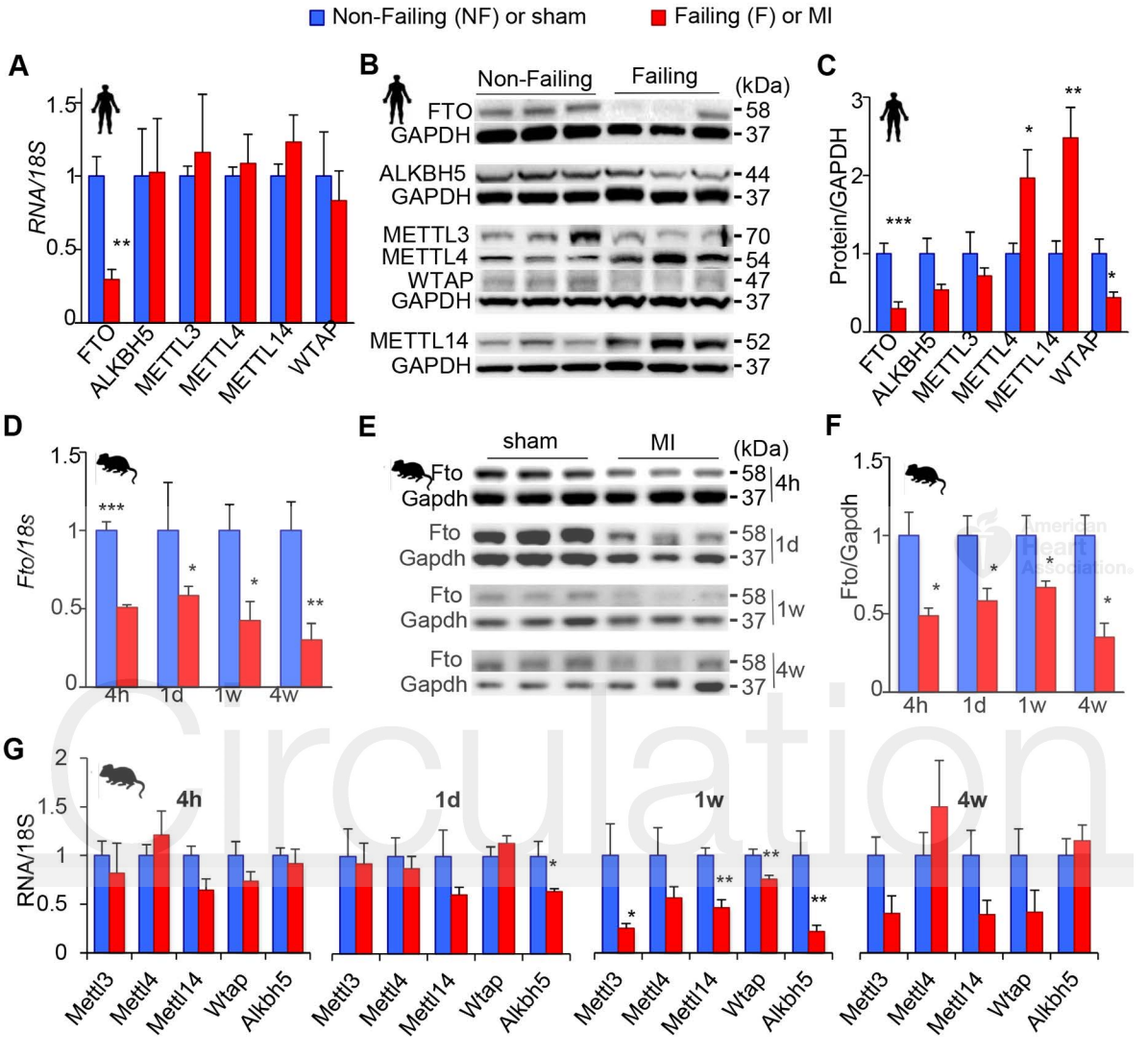

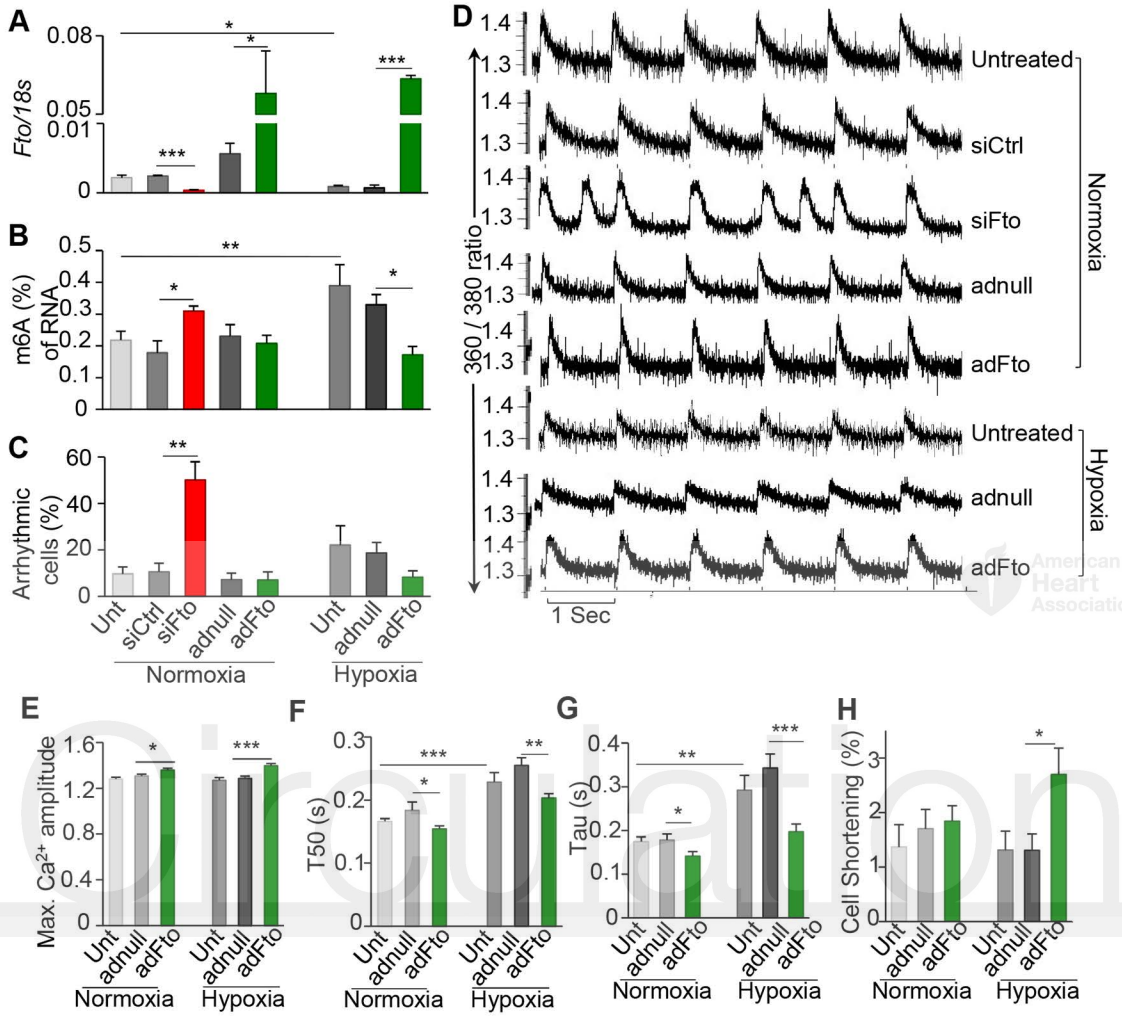

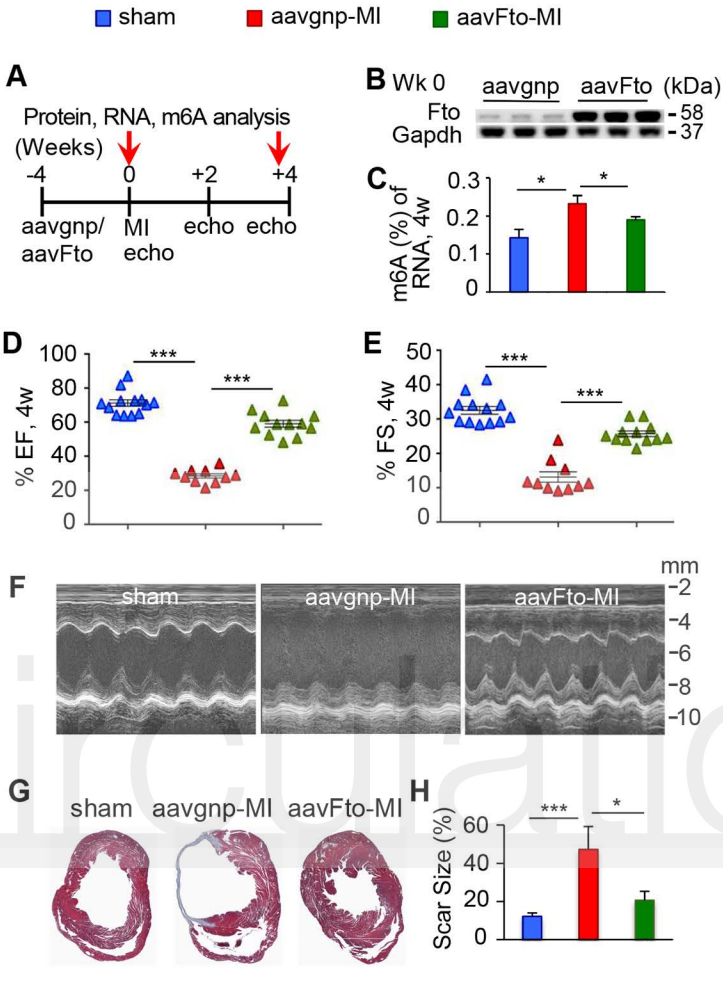

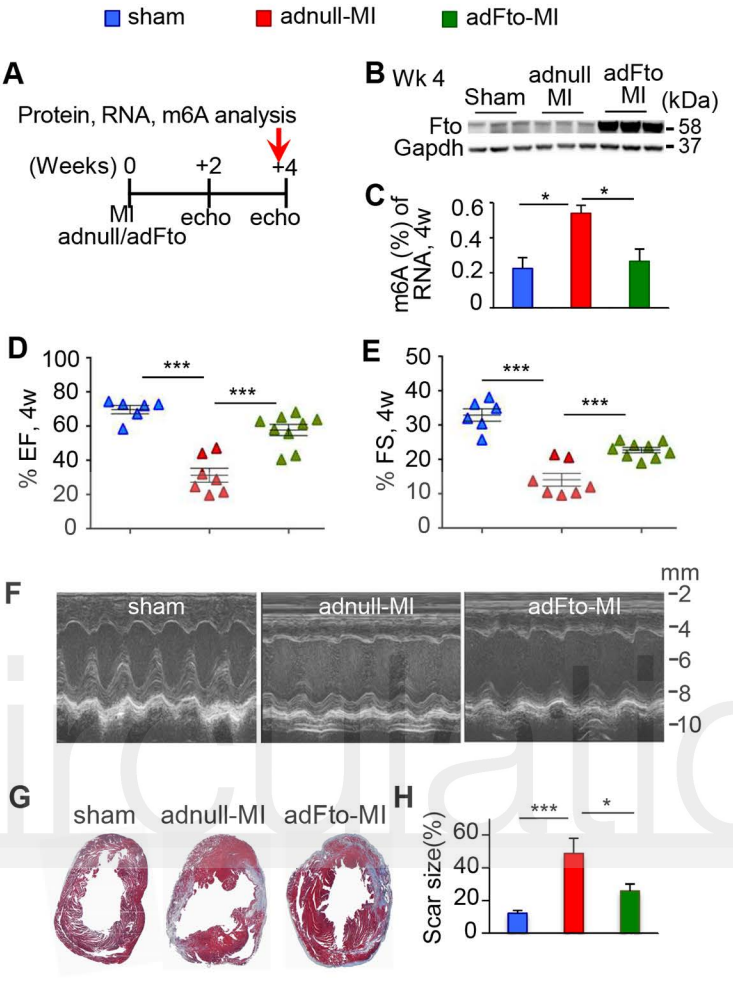

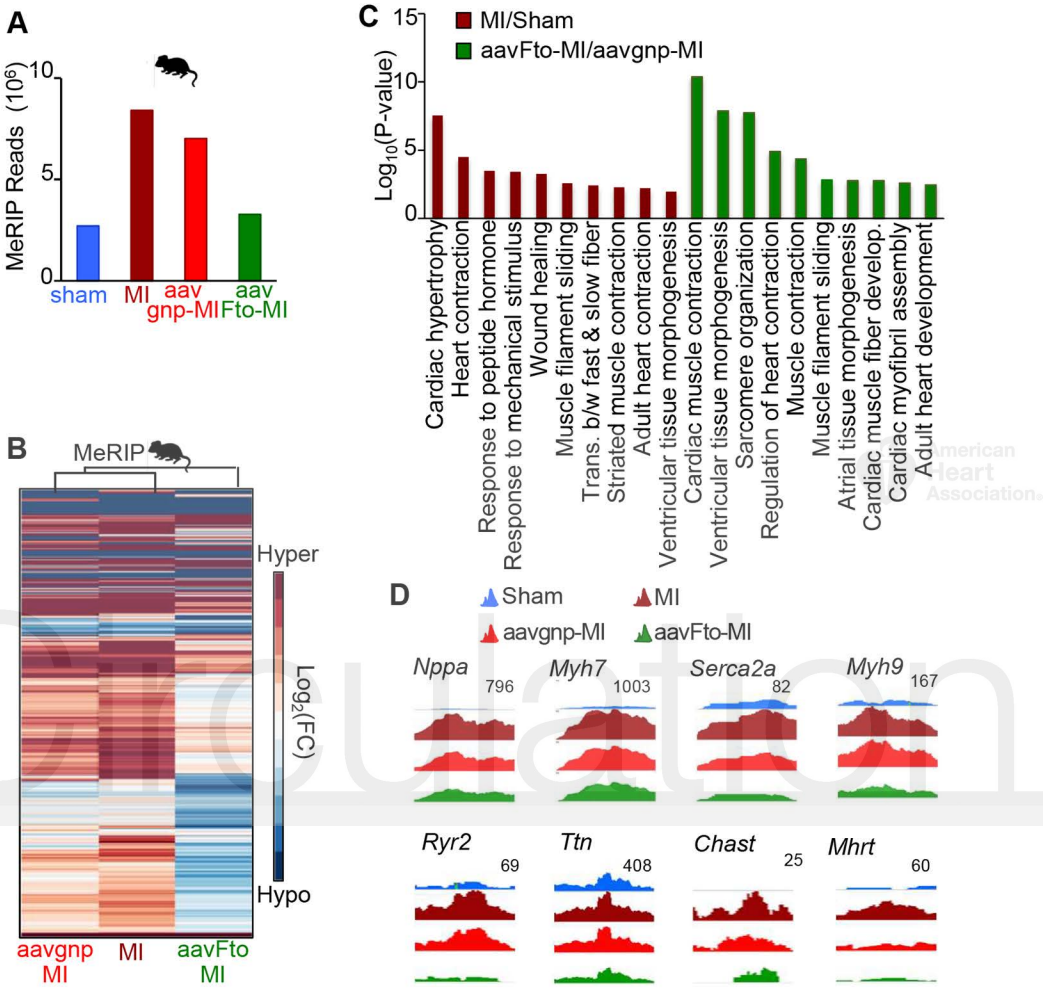

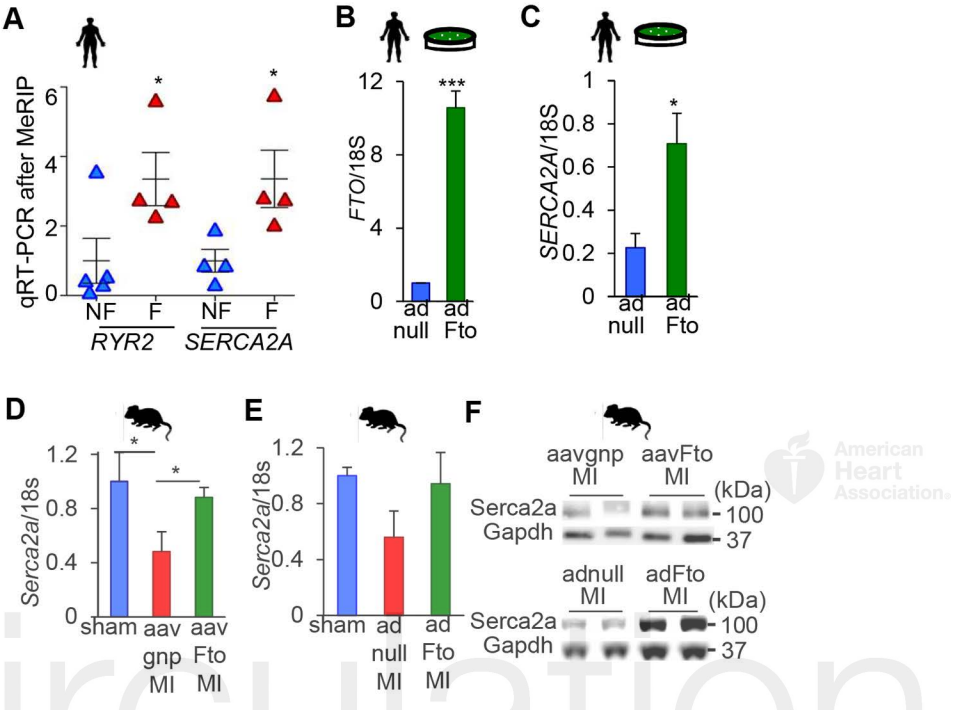

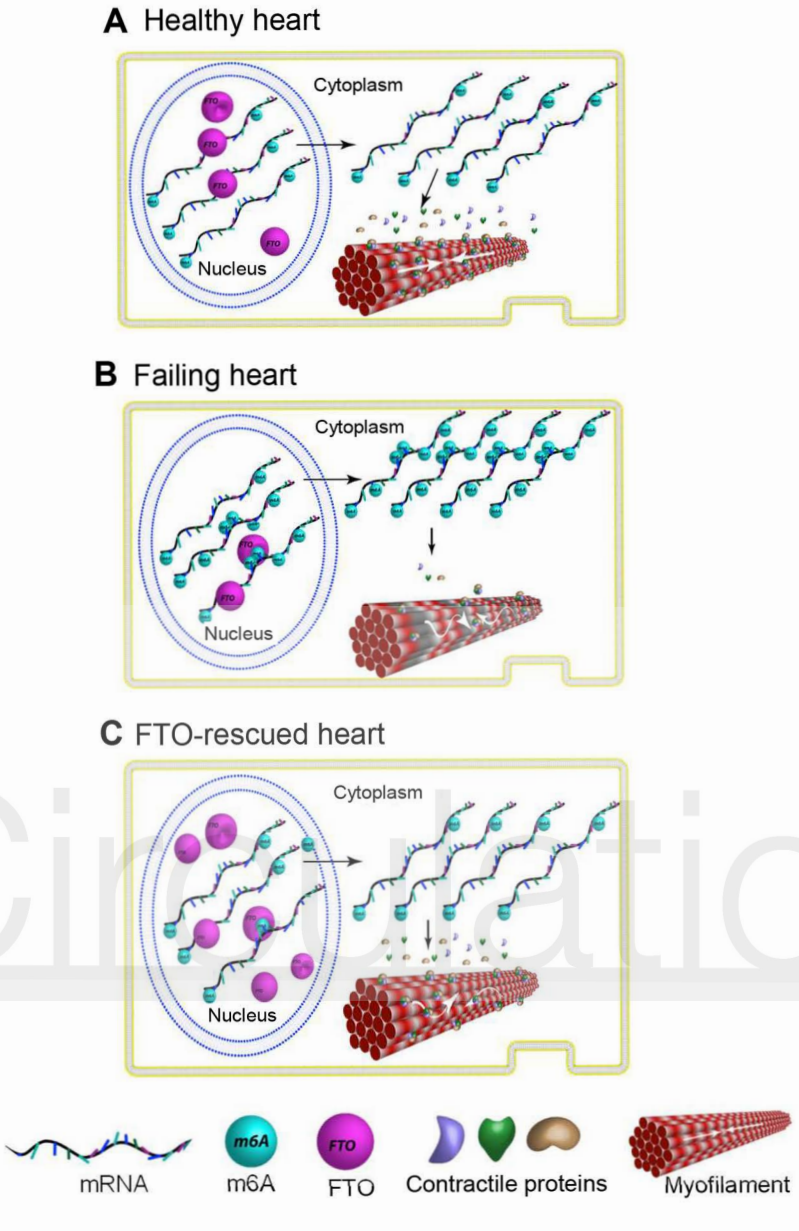

FTO-Dependent m6A Regulates Cardiac Function During Remodeling and Repair

Prabhu Mathiyalagan, Marta Adamiak, Joshua Mayourian, Yassine Sassi, Yaxuan Liang, Neha Agarwal, Divya Jha, Shihong Zhang, Erik Kohlbrenner, Elena Chepurko, Jiqiu Chen, Maria G. Trivieri, Rajvir Singh, Rihab Bouchareb, Kenneth Fish, Kiyotake Ishikawa, Djamel Lebeche, Roger J. Hajjar and Susmita Sahoo

Circulation. published online July 11, 2018;
Circulation is published by the American Heart Association, 7272 Greenville Avenue, Dallas, TX 75231

Print ISSN: 0009-7322. Online ISSN: 1524-4539

SUPPLEMENTAL MATERIAL

Title: FTO-Dependent m6A Regulates Cardiac Function During Remodeling and Repair

Authors

Prabhu Mathiyalagan, PhD, Marta Adamiak, PhD, Joshua Mayourian, PhD, Yassine Sassi, PhD, Yaxuan Liang, PhD, Neha Agarwal, MS, Divya Jha, PhD, Shihong Zhang, BS, Erik Kohlbrenner, BS, Elena Chepurko, DVM, Jiqiu Chen, MD, Maria G. Trivieri, MD, Rajvir Singh, PhD, Rihab Bouchareb, PhD, Kenneth Fish, PhD, Kiyotake Ishikawa, MD, PhD, Djamel Lebeche, PhD, Roger J Hajjar, MD, Susmita Sahoo, PhD

SUPPLEMENTAL MATERIALS AND METHODS

All the experimental protocols are in compliance with the National Institutes of Health Guide for the Care and Use of Laboratory Animals and standards of United States regulatory agencies.

Human Left Ventricular Tissues

To study human ischemic heart failure, we obtained human left ventricular (LV) samples from both male and female donors or explanted hearts at the time of transplantation. Subjects were grouped as non-failing (controls without history of cardiomyopathy; n=10; mean age 54.8 ± 16.4 years) or failing (diagnosed with ischemic/non-ischemic cardiomyopathy; n=11; mean age 54.7 ± 10.2 years). LV tissues were obtained from postmortem failing (with diagnosed cardiomyopathy) and non-failing (with no history of cardiomyopathy and non-cardiac related death) human hearts from National Disease Research Interchange (NDRI). No human subjects are involved; LV tissues were only obtained from deceased individuals. Mount Sinai Institutional Review Board approved procurement of human tissue samples from NDRI. We have used and have proposed to use tissues from de-identified individuals. All usage was as per Mount Sinai approved guidelines. The donors for failing hearts had a history of myocardial infarction and coronary artery disease and samples from individuals with illicit drug use, with chemotherapy and radiation were eliminated. The collected tissues are subjected to HIV/HepB testing before use and are treated as potentially contagious for blood borne pathogens. Appropriate precautions were taken throughout the study.

Myocardial Infarction in Swine

Yorkshire pigs (18-22 kg females) were pre-medicated using intramuscular Telazol (8.0 mg/kg, Fort Dodge, IA). After the placement of an intravenous line, animals were intubated and ventilated with 100% oxygen. General anesthesia was maintained with intravenous propofol (8-

10 mg/kg/hr) throughout the procedure. A bolus of atropine (0.05mg/kg) and amiodarone (1-3 mg/kg) were given intravenously or intramuscularly. A 1000 ml saline bag mixed with atropine (0.1mg/Kg), amiodarone (3mg/kg), and potassium acetate (20mEq) was continuously infused at the rate of 300 ml/hr for the duration of the procedure. A 7-Fr hockey-stick catheter (Cordis) was advanced to the left coronary artery. After the coronary angiogram, a 0.014-inch guide wire (Abbott, Park, IL) was advanced into the LAD and 8-mm-long, 4.0-mm VOYAGER over-the-wire balloon (Abbott) was advanced to the proximal part of the coronary artery. The balloon was then inflated to 3-4 atm for 120 minutes followed by reperfusion. In case of malignant arrhythmia, direct current shock was applied immediately with continuous chest compression. After confirmation of hemodynamic stability, animals were allowed to recover. Intramuscular injections of nitroglycerine and furosemide are administered. Intravenous saline with amiodarone, atropine and potassium acetate infusion is decreased to 50 ml/hr and was given overnight. The animals were housed in their cages, and examined daily for any signs of pain or distress. At 2 weeks (2w), 4 weeks (4w), 12 weeks (12w) and 20 weeks (20w) after MI creation, the pigs were euthanized and the heart was dissected and infarct and non-infarct tissues were snap frozen.

Myocardial Infarction in mice

All our experiments involving mice surgery and echocardiographic assessments were performed in a blinded manner (both the surgeon and the person acquiring/analyzing echo data was blinded to the treatments).For mouse models of ischemic cardiomyopathy, we created myocardial ischemia (MI) by performing permanent ligation of the left anterior descending artery (LAD) in C57BL/6 male mice with body weight from 25-34 g as previously described(*1*). Briefly, animals were anesthetized intraperitoneally with Ketamine 100mg/kg, and Xylazine 10mg/kg. After thoracotomy, ligation of the LAD was performed with a 7-0 silk suture. The successful performance of LAD ligation was verified by visual inspection of color of the apex. The chest

was closed with 6-0 silk sutures, and the skin was closed with 4-0 silk sutures. All mice were housed under identical conditions, and were given water and food ad libitum. LV tissues were harvested for biochemical assays at 4-hour (4h), 1-day (1d), 1-week (1w) and 4-weeks (4w) post-MI or sham surgeries. We collected both infarct/border area and non-infarct (remote) area as distinct regions from LV tissues post LAD ligation and tissues were immediately snap frozen.

Total RNA extraction for cDNA synthesis and real-time PCR

In mouse and swine, LV tissues from sham or MI (infarct and non-infarct) were carefully dissected at different time point's post-MI surgeries and immediately snap frozen. From human failing and non-failing tissues, ~5mg of LV tissues from distinct LV regions were pooled together for RNA or protein preparation. Tissues were resuspended in 700ul Qiazol Lysis Reagent (Qiagen) and homogenized in a RNase/DNase free 2 ml lysing matrix tubes (MP Biomedicals) using tissue homogenizer. Chloroform was added to the tissue homogenate and vortexed briefly before centrifugation at 4^{o}C for 15 minutes at 12,000g. The RNA containing aqueous phase was then collected and total RNA was extracted using miRNeasy mini kit (Qiagen) as recommended by the manufacturer's protocol. RNA was eluted in RNase-free water and quantification of RNA was performed immediately using nanodrop spectrophotometer. RNA was stored as aliquots at -80^{o}C until further use. For gene expression profiling by qRT-PCR, cDNA was synthesized using 1 microgram of total RNA per tissue extract. First strand cDNA synthesis was carried out using high capacity cDNA synthesis kit according to the manufacturer's protocol (Applied Biosystems). qRT-PCR quantification of relative mRNA was determined using Taqman probes (Applied Biosystems). For realtime PCR detection, 2ul of cDNA from each sample was resuspended in a reaction mix to make a final volume of 20ul per PCR reaction. Realtime PCR was carried out as follows: One step of holding (10 min, 95^{o}C), 40 cycles of denaturation (15 sec, 95^{o}C) and extension (1 min, 60^{o}C). For all gene expression profiling, 18S rRNA (HS03003631_G1) was used as internal control and gene expression was normalized to 18S rRNA levels. Taqman

primers for mouse: Fto (Mm00488755_m1); Alkbh5 (Mm00841140_m1); Mettl3 (Mm01316319_m1); Mettl4 (Mm01236354_m1); Mettl14 (Mm01318173_m1); Wtap (Mm00808544_s1); Atap2a2/Serca2a (Mm01201431_m1). For Human: FTO (Hs01057145_m1); ALKBH5 (Hs00539502_m1) METTL3 (Hs00219820_m1) METTL4 (Hs01559838_m1); METTL14 (Hs00383340-m1); WTAP (Hs01695908_s1); ATP2A2/SERCA2A (Hs00544877_m1). For Rats: Fto (Rn01538186_m1).

Western Blotting

For human protein extract, ~5mg tissues from random LV areas from each sample were pooled together. For mouse, ~15mg sham or MI tissues were frozen after sham or MI surgeries at all time points studied. For protein extraction *in vitro* from isolated adult rat primary cardiomyocytes or AC16 myocytes, cells were washed in ice-cold PBS at least twice before centrifugation to obtain cell pellet. Human and mouse tissues as well as cell pellets from culture were resuspended in 1x Pierce RIPA buffer (Thermo Scientific) containing 1x Halt protease inhibitor cocktail (Thermo Scientific). Tissues were homogenized to lysate in 2 ml lysing matrix tubes (MP Biomedicals) using tissue homogenizer. Tissue lysates and cells lysates were incubated in ice for at least 5 minutes to ensure proper cell lysis before centrifugation of lysates at 4^{o}C for 15 minutes at 12,000g. Following centrifugation, soluble supernatant was carefully transferred to a fresh eppendorff tube and protein estimation was carried out using Pierce BCA protein assay (Thermo Scientific). About 20 microgram of protein extract was loaded per lane in a Bolt 4-12% Bis-Tris Plus gel (Invitrogen). For Serca2a blots, protein samples were preheated for 45 minutes at 37^{o}C before loading and for rest of the protein blots, samples were preheated for 5 minutes at 95^{o}C. After protein transfer to PVDF membrane, selected proteins were probed with antibodies as indicated. Antibodies included in this study- FTO (ab92821, Abcam), ALKBH5 (ab174124, Abcam), METTL3 (MT-A70, Bethyl), METTL4 (ab107540, Abcam), METTL14 (ab98166, Abcam), WTAP (sc-374280, Santa Cruz), SERCA2A (sc-8094, Santa Cruz), GAPDH

(ab125247, Abcam). Primary antibody dilutions: FTO (1:500), ALKBH5 (1:250), METTL3 (1:2500), METTL4 (1:500), METTL14 (1:500), WTAP (1:500), SERCA2A (1:3000) and GAPDH (1:2000).

Isolation and culture of adult rat primary cardiomyocytes

For in vitro studies, to obtain sufficient amount of cardiomyocytes to perform IonOptix experiments, qRT-PCR, m6A assays under several treatment conditions (siCtrl/siFto, adnull/adFto, normoxia/hypoxia), we isolated primary cardiomyocytes from adult Sprague-Dawley rats (150-300gr). Both male and female rats were used for cardiomyocyte isolation. Briefly, rats were euthanized with Isoflurane in a gas chamber and hearts were carefully excised with large portion of aorta intact and mounted using a cannula on the Langendorff apparatus. While mounted, hearts were perfused with Tyrode solution containing 2,3-butanedione monoxime (BDM) until the color of the tissue turns pale. Subsequently, hearts were perfused with pre-warmed digestion solution (Collagenase Tyoe II, 1.5mg/ml and Hyaluronidase, 0.1mg/ml in Tyrode buffer) for 50 minutes(*2*). Enzymatic digestion was then stopped using reaction stop solution containing EDTA. Single cell suspension of the LV was then carefully transferred to a final volume of 10ml Tyrode buffer containing BSA (1%) and calcium was slowly introduced for 30 minutes. Cardiomyocytes were allowed to settle down in tubes and supernatant containing non-myocytes were separated. For culturing cardiomyocytes, laminin pre-coated plates were utilized. After attaching cardiomyocytes to laminin for 2 hours in culture media supplemented with 10% FBS, 1% penicillin/streptomyocin and 2,3-Butanedione 2-monoxime (BDM), media was removed gently without disturbing attached myocytes and fresh warm media was added before proceeding to downstream experiments under normoxia or hypoxia conditions.

Hypoxic treatment of isolated adult rat primary cardiomyocytes and human cell lines

After adding fresh media to cardiomyocytes attached to laminin, dishes were either cultured under normoxic or hypoxic conditions. For normoxic culture conditions, dishes were placed in regular cell culture grade incubators and cultured at 37^{o}C with 5% carbon dioxide. For hypoxic culture conditions, cardiomyocytes containing dishes were transferred to a self-contained and sealed hypoxic incubator chamber (Stem Cell technologies) and filled with Nitrogen gas to achieve ~0.1% oxygen inside the chamber. After sealing of the hypoxia incubation chamber filled with Nitrogen gas, the chamber is placed inside regular cell culture incubator at 37^{o}C. After ~16 hours, normoxic and hypoxic cells were analyzed. For RNA and protein, hypoxic chamber was opened and cells were harvested in Qiazol (Qiagen) or in 1x RIPA buffer (with protease inhibitor), respectively. For cardiomyocytes functional assays by IonOptix, hypoxia chamber was opened and measurements were done under normoxic conditions at room temperature. For human cell lines, we cultured AC16 human ventricular myocytes (originally obtained from ATCC), human cardiac fibroblasts (originally obtained from ScienCell Research Laboratories) and Human umbilical vein endothelial cells (HUVECs, originally obtained from Lonza).

Fto knockdown and overexpression in primary cardiomyocytes or human ventricular AC16 cardiomyocytes in vitro

For siRNA-mediated Fto silencing, 20nm siRNA targeting exon 4 of Fto was added to cardiomyocytes in culture and incubated overnight. Lipofectamine RNAiMAX Reagent (Invitrogen) was used as siRNA transfection reagent. Control siRNA (siCtrl) was performed simultaneously as control. For Fto over expression, adenovirus plasmid carrying full-length Fto coding sequence (ADV-259684) and adenovirus null (adnull) control plasmids was purchased from Vector Biolabs; adnull (Vector Biolabs #1300) is the adenovirus containing an empty CMV promoter and served as control. Adeno virus treatment was 100 PFU /cell for primary cardiomyocytes under both normoxia and hypoxia conditions. After 24 hours, cells were washed at least twice before collecting for RNA and protein extraction from all treatment conditions.

Measurements of calcium dynamics and sarcomere contraction in isolated adult rat primary cardiomyocytes

After 16-24 hours of culture, cardiomyocytes were subjected to assessments of intracellular calcium and sarcomere contractile properties. Cardiomyocytes cultured in hypoxia chamber were opened and cell culture dishes containing cardiomyocytes were kept at 37 degrees and all measurements were taken place at room temperature. It is not possible to maintain hypoxic environment during ionoptix measurements of primary cardiomyocytes due to experimental requirements, therefore the in vitro hypoxia experiments likely mimic hypoxia-reoxygenation, which leads to exposure to oxygen prior and during measurements. Briefly, for the Ca^{2+} measurements, cells were incubated at room temperature with 1.5 μM Fura-2 acetoxymethyl ester (Molecular Probes) for 10 min and protected from light. Next, the coverslips containing cardiomyocytes were attached to the stage of an inverted Motic AE31microscope. Sarcomere and Ca^{2+} transients were recorded at 1Hz pacing stimulation frequency with MyoPacer Field Stimulator (IonOptix MA, USA). During the intracellular Ca^{2+} measurements, cardiomyocytes were incubated with the 1.2mM Ca^{2+} and subjected to dual excitation (360/380nm) using a fluorescence photomultiplier system (IonOptix MA, USA) equipped with a xenon lamp. The emission fluorescence was collected at 510nm. Cell shortening was measured using video microscopy motion-detector system (IonOptix MA, USA).

Calcium traces were analyzed using IonWizard Transient Analysis software (IonOptix). Five to six transients from each individual cell were averaged, and characteristics including transient time, baseline, peak, time to peak, peak height, tau, max velocities, max rates, and rate constants were generated by the software. Calcium amplitudes and cell shortening were measured as the peak height of transient. Max Calcium amplitudes were measured as the value of the transient at its maximal deflection from baseline. Times to % peak (T50, T90) were

defined as times for the transient to reach a percent (50% and 90% in the study) of the peak during the deflection phase of the transient. Max velocities were defined as the maximum of first derivative of transient during the deflection and recovery phases of the transient. Tau values were defined as the exponential decay time constant of the function to characterize the speed of recovery (relaxation or calcium reuptake).

Digestion of human LV tissues and isolation of single cell suspension for cardiomyocyte and non-cardiomyocyte fractionation

Frozen human LV tissues collected from non-failing heart donors were thawed in ice and chopped into fine tissue pieces in presence of cold isolation solution (120 mM NaCl, 5.4 mM KCl, 1.4 mM $MgSO_4$, 1.2 mM NaH_2PO_4, 20 mM $NaHCO_3$, 10 mM BDM (2,3-Butanediene monoxine), 5 mM Taurine, 5.6 mM Glucose, 1 mM MgCl2, in H_2O). Fresh collagenase solution was prepared every time by diluting 0.025g of Collagenase type II (Worthington Biochemical, LS004177) in 20 ml of isolation solution containing 0.25 mM $CaCl_2$ per tissue digestion. Finely chopped human LV tissue was transferred to a fresh 50 ml tube containing 20 ml of pre-warmed (37^{o}C) collagenase solution and tissue was pipetted up and down in solution twenty times using 25 ml serological pipette to facilitate digestion. Tubes were then incubated in a 37^{o}C water bath for 10 minutes with swirling every one minute during this incubation. Samples are once again pipetted for twenty times using 25 ml serological pipette and centrifuged at 60g for 1 minute at 4^{o}C. The supernatant containing single cell suspension was collected and 2x Reaction stop solution (X-VIVO 10 medium Lonza, 500 uM EDTA, 0.05% BSA, 0.02mg/ml DNase I) was added followed by centrifugation at 60g for 2 min at 4^{o}C. Supernatant was then centrifuged at 400g for 6 minutes to obtain cell pellet and cells were resuspended in PBS. Whole cell preparation was stored as aliquot and the rest of cell suspension was centrifuged at 60g for 2 minutes. Supernatent was stored for non-cardiomyocyte and pellet was stored for cardiomyocyte analysis. RNA was isolated as described before and equal amount of RNA used

for cDNA synthesis for gene expression comparison.

Adenovirus or Adeno-associated virus production and Fto gene delivery in vivo

AAV cis-plasmid carrying full-length Fto (pAAV-CAG-mFTO) coding sequence was purchased from Vector Biolobas (pAAV-259684). AAV serotype-9 was produced with full-length Fto coding sequence in HEK-293T cells as described previously(*3*). When achieved 60-70% confluency, cell culture medium was supplemented with transfection reagent, which was made by mixing of the helper plasmid, Fto-containing plasmid and polyethylenimine (Polysciences, Warrington, PA) in DMEM supplemented with 2% FBS and streptomycin-penicillin. The cells were collected 3 days later at 300g for 10 minutes and resuspended in 10 ml of lysis buffer (150 mmol/l sodium chloride, 50 mmol/l Tris–HCl pH 8.5), subjected to three freeze-thaw cycles and treated with 1,500 u of Benzonase Nuclease (cat. no. E1014; Sigma-Aldrich) in the presence of 1 mmol/l magnesium chloride for 1 hour at 37 °C. Cellular debris was removed by centrifugation for 10 minutes at 5,000*g* (Sorval RC-4, LH-4000 rotor). The virus was purified by a four-step iodixanol gradient centrifugation in a 70Ti rotor (Beckman Coulter, Brea, CA) at 68,000 r.p.m., for 1 hour using OptiSeal Polyallomer Tubes (cat. no.: 361625; Beckman Coulter). Purified virus was used for in vivo transfection. Capsid protein content and purity were determined by performing SDS-PAGE and Coomassie staining. Infectivity and Fto transgene expression was determined by infecting 293T cells (with helper plasmid co-infection) and western blotting for Fto levels compared to uninfected cells. For aavFto or aavgnp, viruses were injected via tail vein to c57Bl6 mice (before the sham or MI surgery) at a dose of 1e11/mouse. aavgnp (aav plasmid carrying full-length coding sequence of Green Fluorescent Protein but no promoter) served as control. For adenovirus, adenovirus plasmid carrying full-length Fto coding sequence (ADV-259684) and adenovirus null (adnull) control plasmids was purchased from Vector Biolabs. adFto or adnull were injected intramyocardially at a dose of 1e9/mouse. adnull is the adenovirus containing an empty CMV promoter and served as control.

Echocardiography assessment of mouse myocardium

All our experiments involving mice surgery and echocardiographic assessments were performed in a blinded manner (both the surgeon and the person acquiring/analyzing echo data was blinded to the treatments).

Animal preparation: Mice were anesthetized with isoflurane (Baxter Healthcare, USA) at a concentration of 4% (induction) and 1.5% (maintenance) in 100% oxygen using SurgiVet Gas Anesthesia System for echocardiographic scanning. Each animal was placed on a heating table in a supine position with the extremities tied to the table through four electrocardiography leads. The chest was shaved using a chemical hair remover (Veet, Reckitt Benckise, Granollers, Spain). Warmed ultrasound transmission gel (Aquasonic-100, Parker laboratories, USA) was applied to the thorax surface to optimize the visibility of the cardiac chambers. The heart rate (HR) of the animals was recorded immediately before the echocardiographic study and was kept consistent (475±50 bpm) between experimental groups. Core temperature was maintained at 37 °C.

Data acquisition, views and measurements: Transthoracic echocardiography was performed using a Vevo2100 ultrasound system (VisualSonics, Toronto, Canada) equipped with a real time micro-visualization scan head probe (MS-550D) working at a frame rate ranging between 230 and 240 frames per sec (fps). The transducer has a central frequency of 30 MHz. Two-dimensional left ventricular (LV) B-mode images were obtained in the parasternal long-axis view at the level of papillary muscles (as shown in Supplemental Figure 10G). LV trace of parasternal long axis B-mode image (PSLAX) of mice heart in full diastole and full systole was obtained and the ejection fraction (%EF) and fractional shortening (%FS) for each heart was calculated using dedicated Vevo2100 quantification software (VevoLab v. 3.1.1.) that follows a clinically accepted

modified Simpson's biplane method of disks approach for left ventricular analysis. Data were processed using GraphPad software with one-way ANOVA to determine statistical significance.

Immunostaining of mouse heart tissues

At day 28, sham or adenovirus or AAV injected mice were sacrificed, perfused by injecting PBS through LV. Heart was then perfused with 4% PFA. Heart tissues was then transferred to 4% PFA contained in a fresh tube and fixed by leaving tissues at four degrees overnight. Heart tissues were paraffin embedded and cross-sectioned (5 um) for histological immunostaining.

For fibrosis, Masson Trichrome staining was used. Steps were conducted according to manufacturer's recommendations (Abcam, ab150686). Briefly, tissues were deparaffinized by heating at 37^{o}C for 5 min followed by three washes of Xylene and four washes of ethanol (96%, 80%, 70%, 50%) for 3 min and tissues were hydrated with distilled water for 10 min. Slides were placed in preheated Bouin's Fluid for 60 min at 56-64^{o}C in a fume hood followed by a 10 minute cooling period. After two times of washing with distilled water, slides were stained with Weigert's Iron Hematoxylin for 5 minutes followed by washing with water. Biebrich Scarlet / Acid Fuchsin solution was then applied onto each section for 15 minutes followed by Phosphomolybdic/Phosphotungstic Acid solution for 10 minutes and Aniline Blue solution for 8 minutes and washed with distilled water. Slides were then incubated in acetic acid solution (1%) for 3-5 minutes and dehydrated in 2 changes of 95% ethanol followed by 2 changes of absolute ethanol. Slides were then incubated in Xylene and mounted in synthetic resin. For quantification, whole heart images were quantified using ImageJ and percent (%) of fibrosis was presented as infarct area (%) to whole LV area.

For angiogenesis, anti-CD31 immunostaining was performed. Briefly, after deparaffinization, heat-induced antigen retrieval was carried out in citrate buffer pH 6.0 (Antigen Retriever, Sigma-

Aldrich) for 45 min at 98°C followed by cooling at room temperature for 45 minutes. After three washes with distilled water, tissue sections were hydrated with PBS for 10 minutes. Blocking buffer (2% nonfat milk, 5% FBS, 0.5% Triton X-100 in PBS) was added for 45 minutes followed by incubation with anti-CD31 primary antibody (Abcam, ab28364) overnight at 4°C in a humid chamber. After washing with PBS (3x), tissue sections were incubated with secondary antibody (Invitrogen, A-21428) for 30 min at room temperature followed by washing with PBS (3x). Nuclei were counterstained using DAPI (4',6-diamidino-2-phenylindole, Vector Laboratories) followed by washing with PBS (3x) and mounting using 50/50 PBS/glycerol mixture. For quantification of immunostaining, tissues were imaged using confocal fluorescence microscopy and CD31-positive cells were quantified from at least six images collected from two sections per condition for comparison between groups. At least three hearts were sectioned per condition and data was presented as the average number of CD31-positive staining per condition. For image presentation, only brightness and contrast adjustments were made and all images were processed similarly between all groups for presentation.

SUPPLEMENTAL TABLES

Table. S1. Differential m6A peaks obtained from MeRIP analysis of MI relative to Sham. Hypermethylated (>2 fold change) and demethylated (<0.5 fold change) transcripts are listed. Inclusion of formal FDR control can be found in Table. S5.

	Gene	chr	Fold Change		Gene	chr	Fold Change
1	Nppa	chr4	148.0560875	**59**	RRBP1	chr2	3.758090997
2	COL3A1	chr1	144.007486	**60**	HSP90B1	chr10	3.317278183
3	POSTN	chr3	95.67035191	**61**	CDH5	chr8	3.138336392
4	SPARC	chr11	87.42657643	**62**	GOLGA4	chr9	3.138336392
5	Nppa	chr4	66.71780869	**63**	HSPA5	chr2	3.052518418
6	Nppa	chr4	66.71780869	**64**	NEAT1	chr19	2.989698497
7	COL1A2	chr6	49.8665331	**65**	tuba4a	chr1	2.969047141
8	COL3A1	chr1	44.01733818	**66**	NRAP	chr19	2.928171392
9	BGN	chrX	34.7755156	**67**	Neat1	chr19	2.928171392
10	SPARC	chr11	33.8245773	**68**	ACTN2	chr10	2.907945035
11	NPPA	chr4	22.94328397	**69**	ATP5B	chr13	2.907945035
12	MYH12	chr14	21.40684088	**70**	ANP32B	chr4	2.848100391
13	CLU	chr14	20.96629446	**71**	POPDC2	chr16	2.828427125
14	Nppa	chr4	20.96629446	**72**	EIF3A	chr19	2.732080514
15	Nppa	chr4	20.96629446	**73**	COX6A2	chr7	2.67585511
16	MYH11	chr14	20.39297004	**74**	KIF1C	chr11	2.67585511
17	COL1A1	chr11	19.8353232	**75**	ACOT13	chr13	2.67585511
18	SERPINH1	chr7	19.42711815	**76**	cyb5r3	chr15	2.67585511
19	SERPINH1	chr7	15.34822591	**77**	TPM1	chr9	2.584705661
20	MYH10	chr14	15.03236399	**78**	ACTN2	chr13	2.566851795
21	COL4A1	chr8	13.92880901	**79**	ARGLU1	chr8	2.531513188
22	MYH9	chr14	13.92880901	**80**	HRC	chr7	2.4794154
23	MYH8	chr14	12.38051995	**81**	HSPB6	chr7	2.462288827
24	ITGB5	chr16	11.63178014	**82**	NEAT1	chr19	2.445280555
25	APOE	chr7	11.39240156	**83**	NDUFB8	chr19	2.428389769
26	ANKRD3	chr19	11.08087574	**84**	Neat1	chr19	2.411615655
27	CASQ2	chr3	10.26740718	**85**	AHNAK	chr19	2.394957409
28	MYH12	chr15	9.781122222	**86**	Neat1	chr19	2.394957409
29	SPARC	chr11	9.579829637	**87**	CSRP3	chr7	2.37841423
30	MYH11	chr15	8.876555777	**88**	POPDC2	chr16	2.329467173
31	CLU	chr14	8.6938789	**89**	CDK11B	chr4	2.281527432
32	MYH10	chr15	8.339726087	**90**	ART1	chr7	2.234574276
33	HSP90AB1	chr17	7.516181994	**91**	ANP32A	chr8	2.173469725
34	HSPG2	chr4	7.210003701	**92**	NDUFB7	chr9	2.173469725
35	MYH9	chr15	6.727171322	**93**	NDUFB9	chr10	2.099433367
36	MYH7	chr14	6.498019171	**94**	CHCHD10	chr15	2.099433367
37	CST3	chr2	6.408559021	**95**	BAG1	chr4	2.070529848
38	PDGFRB	chr18	5.979396995	**96**	CRIP2	chr12	2.070529848
39	ENG	chr2	5.897076869	**97**	NDRG2	chr14	2.042024251
40	EIF4G1	chr16	5.897076869	**98**	CRYAB	chr9	2.02791896
41	CLU	chr14	5.578974665	**99**	Rn45s	chr17	0.496546248
42	COL4A1	chr8	5.502167273	**100**	Rn45s	chr17	0.453759578
43	ANKRD2	chr19	5.278031643	**101**	ATP2A2	chr5	0.441351498
44	ANKRD1	chr19	5.13370359	**102**	Cox7a1	chr7	0.397768242
45	TMSB4X	chrX	4.924577653	**103**	AES	chr10	0.381564802
46	HSPB7	chr4	4.59479342	**104**	ATP5B	chr10	0.378929142
47	PTMS	chr6	4.563054863	**105**	Lpl	chr8	0.373712312
48	CTSD	chr7	4.469148552	**106**	ATP5B	chr10	0.358488812
49	jund	chr8	4.438277888	**107**	MYBPC3	chr2	0.351111219
50	APP	chr16	4.407620464	**108**	MYOM1	chr17	0.334481889
51	MHRT	chr14	4.377174805	**109**	DSP	chr13	0.320856474
52	APP	chr16	4.34693945	**110**	HRC	chr7	0.314253344
53	CLU	chr14	4.112455307	**111**	LPL	chr8	0.277392368
54	RRP1	chr10	4	**112**	MYBPC3	chr2	0.273573425
55	FABP4	chr3	3.944930818	**113**	OGDH	chr11	0.262429171
56	FTH1	chr19	3.944930818	**114**	MYBPC3	chr2	0.228457863
57	SNRNP70	chr2	3.810551992	**115**	MYH6	chr14	0.169575541
58	XIRP2	chr7	3.810551992	**116**	ATP2A2	chr5	0.065607293

Table. S2. Pathway analysis using differential m6A peaks obtained from MeRIP analysis of MI relative to Sham. Both hypermethylated (>2 fold change) and demethylated (<0.5 fold change) regions included. Top 40 GO terms ranked based on P-Values are listed. Inclusion of formal FDR control can be found in Table. S6.

	Term	PValue	Fold Enrichment
1	GO:0002027~regulation of heart rate	3.42E-07	40.18222222
2	GO:0060048~cardiac muscle contraction	1.49E-06	30.13666667
3	GO:0045214~sarcomere organization	7.48E-06	38.88602151
4	GO:0042060~wound healing	4.14E-05	15.38893617
5	GO:0014898~cardiac muscle hypertrophy in response to stress	5.14E-05	53.5762963
6	GO:0006936~muscle contraction	5.16E-05	24.10933333
7	GO:0002026~regulation of the force of heart contraction	1.10E-04	41.92927536
8	GO:0055010~ventricular cardiac muscle tissue morphogenesis	2.00E-04	34.44190476
9	GO:0007179~TGF beta receptor signaling pathway	2.52E-04	16.07288889
10	GO:0030049~muscle filament sliding	3.42E-04	103.3257143
11	GO:0030199~collagen fibril organization	5.41E-04	24.72752137
12	GO:0032355~response to estradiol	7.82E-04	11.93531353
13	GO:0071356~cellular response to tumor necrosis factor	0.001075354	10.95878788
14	GO:0006898~receptor-mediated endocytosis	0.001904576	16.07288889
15	GO:0071560~cellular response to TGF beta stimulus	0.001997242	15.80939891
16	GO:0001568~blood vessel development	0.003080485	13.582723
17	GO:0043434~response to peptide hormone	0.003332675	13.21059361
18	GO:0006937~regulation of muscle contraction	0.003953959	31.44695652
19	GO:0071260~cellular response to mechanical stimulus	0.004017411	12.36376068
20	GO:0008016~regulation of heart contraction	0.005427893	26.78814815
21	GO:0001666~response to hypoxia	0.007952083	6.278472222
22	GO:1900221~regulation of beta-amyloid clearance	0.008168412	241.0933333
23	GO:1990036~calcium ion import into sarcoplasmic reticulum	0.008168412	241.0933333
24	GO:1903919~negative regulation of actin filament severing	0.008168412	241.0933333
25	GO:0043066~negative regulation of apoptotic process	0.00835791	3.407679623
26	GO:0001501~skeletal system development	0.009633992	9.012834891
27	GO:0014911~positive regulation of smooth muscle cell migration	0.011102296	18.54564103
28	GO:0001649~osteoblast differentiation	0.011168453	8.534277286
29	GO:0030198~extracellular matrix organization	0.01143712	8.459415205
30	GO:0046034~ATP metabolic process	0.01165594	18.082
31	GO:0007155~cell adhesion	0.014398141	3.479697595
32	GO:0017038~protein import	0.016270996	120.5466667
33	GO:0001525~angiogenesis	0.016654085	5.043793584
34	GO:0051591~response to cAMP	0.018510797	14.18196078
35	GO:0071230~cellular response to amino acid stimulus	0.01865655	7.039221411
36	GO:0043588~skin development	0.023563035	12.47034483
37	GO:0042542~response to hydrogen peroxide	0.023563035	12.47034483
38	GO:0043462~regulation of ATPase activity	0.024308275	80.36444444
39	GO:0032964~collagen biosynthetic process	0.024308275	80.36444444
40	GO:1901017~negative reg. of K+ ion transmembrane transporter	0.024308275	80.36444444

Table. S3. Differential m6A peaks obtained from MeRIP analysis of aavFto-MI relative to aavCtrl-MI. Top 20 genes that were demethylated (<0.5 fold change) or hypermethylated (>2 fold change) in aavFto-MI relative to aavCtrl-MI are listed. Inclusion of formal FDR control can be found in Table. S7.

Demethylated transcripts			
	Gene	**chr**	**Fold Change**
1	SERPINH1	chr7	0.174342958
2	FN1	chr1	0.188155843
3	FSTL1	chr16	0.210224104
4	NEXN	chr6	0.223756268
5	RRBP1	chr10	0.236514412
6	TTN	chr2	0.251738888
7	Rn45s	chr4	0.251738888
8	RRBP2	chr2	0.258816231
9	PTRF	chr11	0.262429171
10	CTSB	chr14	0.26425451
11	PLEC	chr15	0.267943366
12	ACOT13	chr13	0.279321785
13	TTN	chr2	0.285190929
14	LAMP1	chr8	0.293208737
15	COL4A1	chr8	0.303548721
16	CCDC80	chr16	0.309926925
17	NDUFB10	chr12	0.318640157
18	NFE2L1	chr11	0.323088208
19	AEBP1	chr2	0.329876978
20	BGN	chr11	0.329876978
Hypermethylated transcripts			
	Gene	**chr**	**Fold Change**
1	ATP5B	chr10	6.543216468
2	cyb5r3	chr15	5.979396995
3	EEF1A2	chr5	5.241573615
4	ATP2A2	chr2	5.241573615
5	CENPB	chr2	5.028053498
6	HSP90AB1	chr17	4.789914818
7	ACO2	chr15	4.789914818
8	MYH9	chr14	4.75682846
9	TCAP	chr11	4.198866734
10	GOLGA4	chr9	3.863745316
11	CKM	chr7	3.810551992
12	NDUFB7	chr8	3.784230587
13	ATP2A2	chr5	3.758090997
14	MYH8	chr14	3.732131966
15	ATP2A2	chr5	3.655325801
16	ATP5G3	chr2	3.60500185
17	AHNAK	chr19	3.580100284
18	GJA1	chr10	3.340351678
19	PDE4DIP	chr3	3.249009585
20	ATP5B	chr16	3.160165247

Table. S4. Pathway analysis using differential m6A peaks obtained from MeRIP analysis of aavFto-MI relative to aavCtrl-MI. *Only demethylated transcripts (<0.5 fold change) in aavFto-MI were included for analysis*. Inclusion of formal FDR control can be found in Table. S8.

	Term	PValue	Fold Enrichment
1	GO:0007044~cell-substrate junction assembly	1.08E-04	177.8557377
2	GO:0001525~angiogenesis	1.38E-04	8.681939776
3	GO:0048739~cardiac muscle fiber development	2.99E-04	111.1598361
4	GO:0010880~regulation of release of sequestered calcium ion into cytosol by sarcoplasmic reticulum	0.001426095	52.31051109
5	GO:0070208~protein heterotrimerization	0.001785471	46.8041415
6	GO:0006937~regulation of muscle contraction	0.00261923	38.66429081
7	GO:0035987~endodermal cell differentiation	0.003602966	32.93624772
8	GO:0006874~cellular calcium ion homeostasis	0.004469978	11.85704918
9	GO:0045214~sarcomere organization	0.004732704	28.68640931
10	GO:0030336~negative regulation of cell migration	0.005258685	11.18589545
11	GO:0001649~osteoblast differentiation	0.006278596	10.49296388
12	GO:0030198~extracellular matrix organization	0.006433241	10.40092033
13	GO:0030199~collagen fibril organization	0.007414668	22.80201765
14	GO:0010649~regulation of cell communication by electrical coupling	0.009922203	197.6174863
15	GO:0001558~regulation of cell growth	0.015887936	15.33239118
16	GO:0007155~cell adhesion	0.022189228	3.667128612
17	GO:0007016~cytoskeletal anchoring at plasma membrane	0.02300135	84.69320843
18	GO:0007584~response to nutrient	0.024472409	12.18189984
19	GO:0071711~basement membrane organization	0.026244499	74.10655738
20	GO:0060316~positive regulation of ryanodine-sensitive calcium-release channel activity	0.026244499	74.10655738
21	GO:0010881~regulation of cardiac muscle contraction by regulation of the release of sequestered calcium ion	0.026244499	74.10655738
22	GO:0030334~regulation of cell migration	0.027018996	11.54907388
23	GO:0086036~regulation of cardiac muscle cell membrane potential	0.029477062	65.87249545
24	GO:0043568~positive regulation of insulin-like growth factor receptor signaling pathway	0.035910561	53.89567809
25	GO:0060306~regulation of membrane repolarization	0.035910561	53.89567809
26	GO:0045822~negative regulation of heart contraction	0.035910561	53.89567809
27	GO:0043066~negative regulation of apoptotic process	0.039387582	3.142327521
28	GO:0044342~type B pancreatic cell proliferation	0.04230212	45.60403531
29	GO:0086004~regulation of cardiac muscle cell contraction	0.051811407	37.05327869
30	GO:0045766~positive regulation of angiogenesis	0.061142985	7.349410649
31	GO:0021591~ventricular system development	0.064346158	29.64262295
32	GO:0002026~regulation of the force of heart contraction	0.073640152	25.77619387
33	GO:0071230~cellular response to amino acid stimulus	0.075894188	6.491085318
34	GO:0010906~regulation of glucose metabolic process	0.079785652	23.71409836
35	GO:0030036~actin cytoskeleton organization	0.080715865	6.262525976
36	GO:0050790~regulation of catalytic activity	0.08284335	22.80201765
37	GO:0006913~nucleocytoplasmic transport	0.097982612	19.12427287

Table. S5. Differential m6A peaks obtained from Exomepeak MeRIP analysis of MI relative to Sham (±2 fold change and FDR<0.05).

chr	chromStart	chromEnd	Entrez_ID	FDR	p-value	fold change
chr5	122469634	122471198	11938	0.028840315	0.001819701	0.065607293
chr14	54963629	54965476	17888	0.026915348	0.00162181	0.169575541
chr14	54973964	54974290	791403	0.036307805	0.002630268	4.377174805
chr19	36112084	36112294	107765	0.032359366	0.002187762	5.13370359
chr19	36116816	36119368	107765	0.00047863	1.31826E-05	5.278031643
chr14	54979349	54980347	140781	0.03801894	0.002884032	6.498019171
chr11	55398663	55406575	20692	0.085113804	0.00724436	9.579829637
chr14	54975959	54979230	140781	0.00047863	1.41254E-05	12.38051995
chr14	54973934	54974749	140781	8.91251E-05	1.90546E-06	13.92880901
chr14	54983244	54983638	140781	0.000812831	2.75423E-05	15.03236399
chr11	94950884	94951575	12842	2.0893E-09	7.94328E-12	19.8353232
chr14	54971695	54972783	140781	1.25893E-05	2.13796E-07	20.39297004
chr4	148001026	148001411	NA	0.002344229	9.77237E-05	20.96629446
chr4	148001025	148001656	NA	0.002344229	9.77237E-05	20.96629446
chr4	148000751	148002074	230899	9.12011E-06	1.1749E-07	22.94328397
chr4	148000790	148000939	NA	0.020892961	0.001148154	66.71780869
chr4	148000790	148000938	NA	0.020892961	0.001148154	66.71780869
chr1	45338737	45339973	12825	0.014125375	0.000660693	144.007486

Table. S6. Pathway analysis using differential m6A peaks obtained from MeRIP analysis of MI relative to Sham (±2 fold change and FDR<0.05).

Term	PValue	FDR	negative log (p-value)
GO:0014898~cardiac muscle hypertrophy in response to stress	2.89E-08	3.50E-05	7.538839216
GO:0002026~regulation of the force of heart contraction	3.24E-05	0.039169155	4.489781014
GO:0043434~response to peptide hormone	3.33E-04	0.40245459	3.477283346
GO:0071260~cellular response to mechanical stimulus	3.80E-04	0.459337839	3.419754293
GO:0042060~wound healing	5.52E-04	0.665979664	3.258012006
GO:0030049~muscle filament sliding	0.002707181	3.22704847	2.56748275
GO:0014883~transition between fast and slow fiber	0.003865477	4.578362818	2.412796954
GO:0006941~striated muscle contraction	0.005408077	6.35114864	2.266957119
GO:0007512~adult heart development	0.006178609	7.225296655	2.209109264
GO:0055010~ventricular cardiac muscle tissue morphogenesis	0.010791066	12.30338783	1.966935657
GO:0002027~regulation of heart rate	0.013855833	15.53516321	1.858367375
GO:0030199~collagen fibril organization	0.01500302	16.71649251	1.823821316
GO:0046034~ATP metabolic process	0.015385161	17.10662903	1.812897945
GO:0060048~cardiac muscle contraction	0.018437721	20.16339108	1.734292757
GO:0006936~muscle contraction	0.019199592	20.91000996	1.716707991
GO:0051591~response to cAMP	0.019580338	21.28072773	1.708179818
GO:0043588~skin development	0.022242011	23.82810698	1.652825952
GO:0071560~cellular response to transforming growth factor beta stimulus	0.02338083	24.8947423	1.631140069
GO:0008217~regulation of blood pressure	0.023760184	25.24699689	1.624150198
GO:0001568~blood vessel development	0.027168688	28.34470646	1.56593133
GO:0034097~response to cytokine	0.030943946	31.63798195	1.509424299
GO:0001501~skeletal system development	0.040700903	39.51678849	1.390395961
GO:0071356~cellular response to tumor necrosis factor	0.041821267	40.36602821	1.378602811
GO:0071230~cellular response to amino acid stimulus	0.051854184	47.49779001	1.285216193
GO:0007507~heart development	0.09678353	70.82174346	1.014198542

Table. S7. Differential m6A peaks obtained from MeRIP analysis of aavFto-MI relative to aavgnp-MI (±2 fold change and FDR<0.05).

chr	chromStart	chromEnd	Entrez_ID	FDR	p-value	Fold change
chr2	91118203	91135443	17868	0.030902954	0.00042658	2.056227653
chr14	54948646	54956941	17888	8.12831E-10	3.16228E-12	2.070529848
chr17	39846482	39846819	NA	0.089125094	0.001737801	2.070529848
chr5	122100979	122106854	17906	0.006456542	6.91831E-05	2.219138944
chr1	135836393	135852268	21956	1.58489E-11	3.98107E-14	2.361985323
chr17	39847897	39848199	NA	3.01995E-05	1.94984E-07	2.514026749
chr17	39847418	39847479	NA	0.042657952	0.00074131	2.713208655
chr11	98383840	98384953	21393	0.030902954	0.000457088	4.198866734

Table. S8. Pathway analysis using differential m6A peaks obtained from MeRIP analysis of aavFto-MI relative to aavgnp-MI (±2 fold change and FDR<0.05).

Term	PValue	FDR	negative log (p-value)
GO:0060048~cardiac muscle contraction	4.37E-11	4.23E-08	10.3595323
GO:0055010~ventricular cardiac muscle tissue morphogenesis	1.33E-08	1.29E-05	7.876562851
GO:0045214~sarcomere organization	1.82E-08	1.76E-05	7.739231156
GO:0008016~regulation of heart contraction	1.29E-05	0.01243938	4.890781579
GO:0006936~muscle contraction	4.48E-05	0.043334125	4.348690125
GO:0030049~muscle filament sliding	0.001547731	1.487258595	2.810304622
GO:0055009~atrial cardiac muscle tissue morphogenesis	0.001768688	1.697957288	2.752348708
GO:0048739~cardiac muscle fiber development	0.001768688	1.697957288	2.752348708
GO:0055003~cardiac myofibril assembly	0.002652152	2.536370758	2.576401582
GO:0007512~adult heart development	0.003535029	3.367816696	2.451606984
GO:0014898~cardiac muscle hypertrophy in response to stress	0.003976248	3.780944477	2.400526533
GO:0002026~regulation of the force of heart contraction	0.005078654	4.806250795	2.294251387
GO:0002027~regulation of heart rate	0.007940626	7.422491231	2.10014524
GO:0003007~heart morphogenesis	0.0140839	12.82178498	1.851277072
GO:0007507~heart development	0.056503463	43.03099563	1.247924932

SUPPLEMENTAL FIGURES

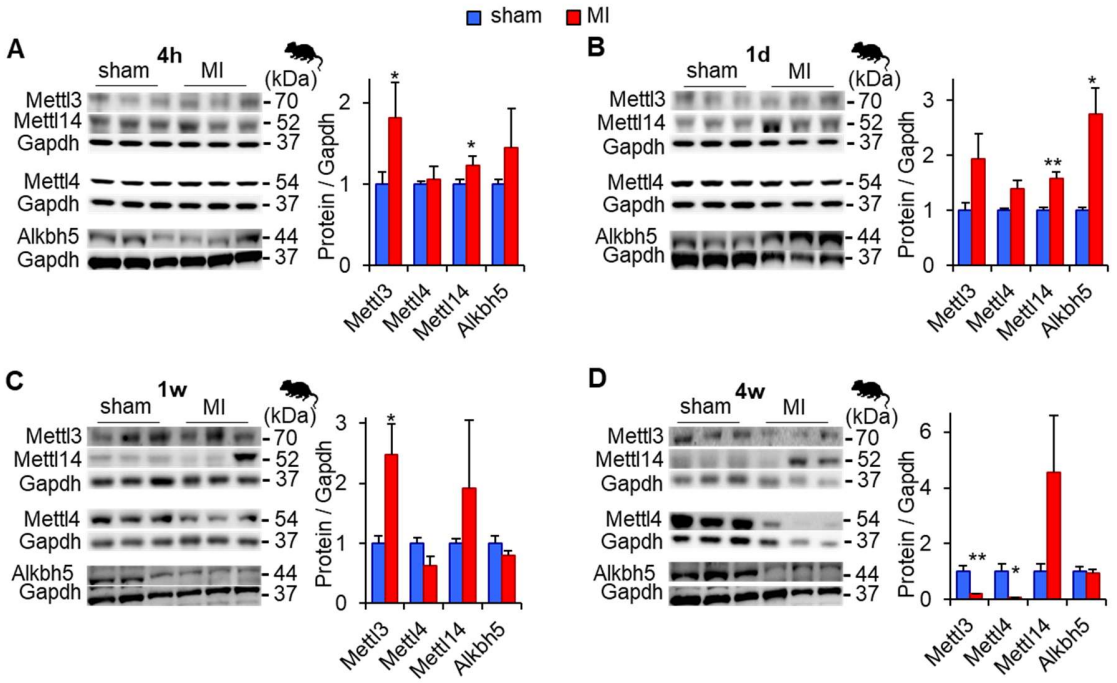

Supplemental Figure 1. Protein analysis for m6A regulators in mouse LV post-MI. Representative immunoblots and densitometry quantifications of selected proteins in mouse LV at **A**, 4h, **B**, 1d, **C**, 1w and **D**, 4w, n=3-5. Error bars represent SEM. **P*<0.05, ***P*<0.01

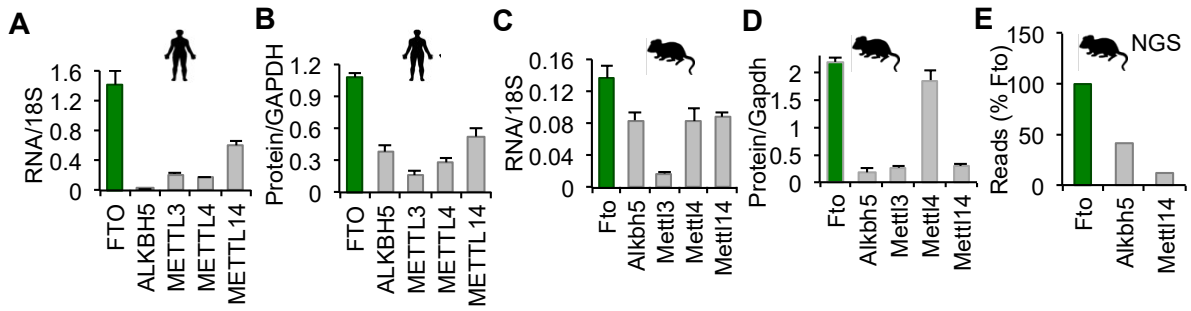

Supplemental Figure 2. Baseline protein and RNA expression for m6A regulators in healthy hearts. Baseline expressions of **A**, mRNA, n=3-6, **B**, protein (from Fig. 2B), n=5, for m6A regulators in non-failing human LV only. Baseline expressions of **C**, mRNA, n=5, **D**, protein, n= 3, for m6A regulators in wild type mouse LV only (without sham or MI surgery). **E**, Total number of read counts detected for m6A regulators by NGS in sham (1w, non-IP) representing the level of mRNA abundance (Mettl 3 and 4 read counts were negligible in NGS data), bars are scaled to Fto reads. Error bars represent SEM.

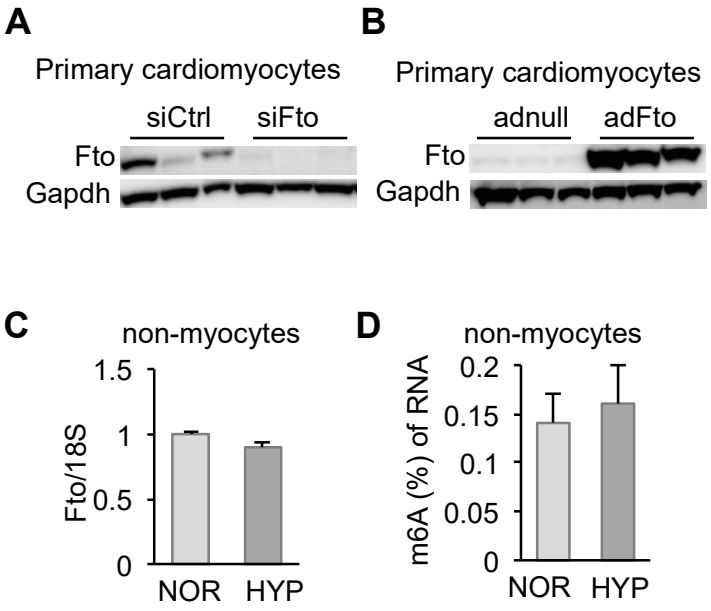

Supplemental Figure 3. RNA and protein analysis in isolated adult rat primary cardiomyocytes and non-myocytes in vitro. Immunoblots showing Fto protein levels after **A**, siRNA-mediated Fto knockdown (siFto), **B**, adenovirus-mediated Fto overexpression (adFto) in isolated primary cardiomyocytes. Quantification of **C**, Fto mRNA, n=4, **D**, m6A % in total RNA, n=4, in non-myocytes isolated from adult rats. Abbreviations, NOR- Normoxia, HYP- Hypoxia. Error bars represent SEM.

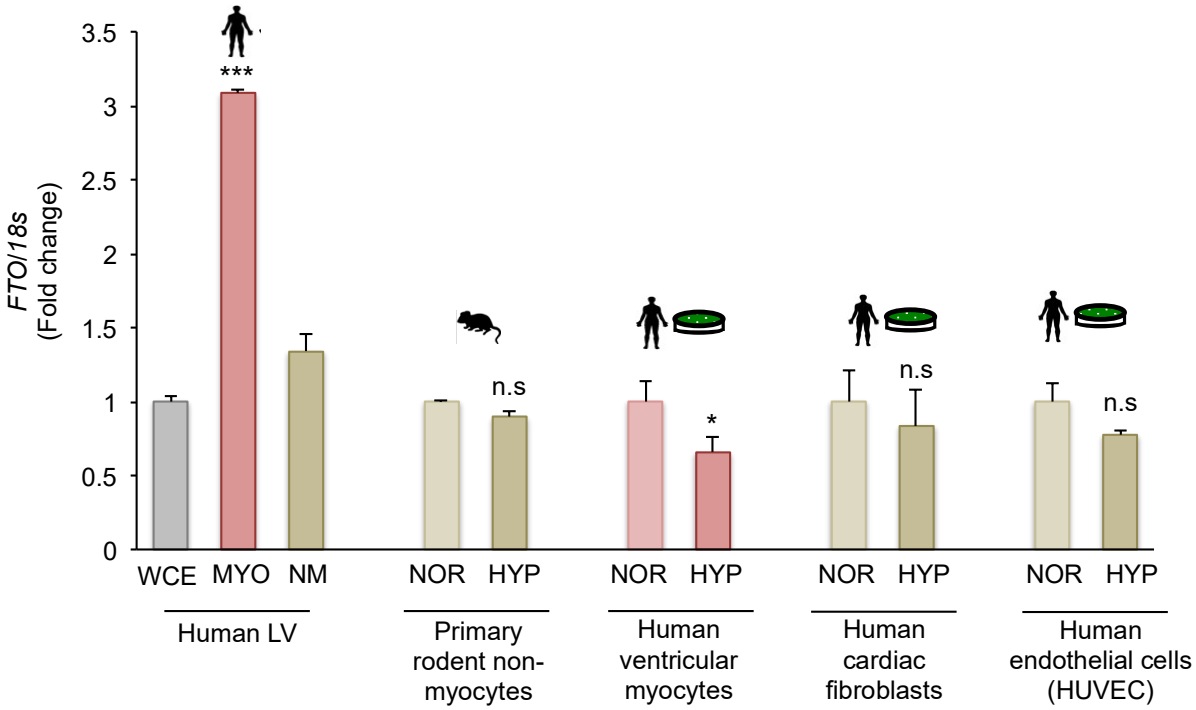

Supplementary Figure 4. FTO expression is more abundant in human myocytes and is significantly downregulated in myocytes under hypoxia culture conditions as compared to non-myocyte cell types. For human LV, tissue was collagenase digested, followed by RNA extraction from whole cell extract (WCE), myocytes (Myo) and non-myocytes (NM) fractions. Equal amount of RNA was used for cDNA and PCR. For cells, normoxia or hypoxia conditions were carried out for ~16 hours before RNA extraction was performed. n = 3-5. Error bars represent SEM. *P<0.01, ***P<0.0001.

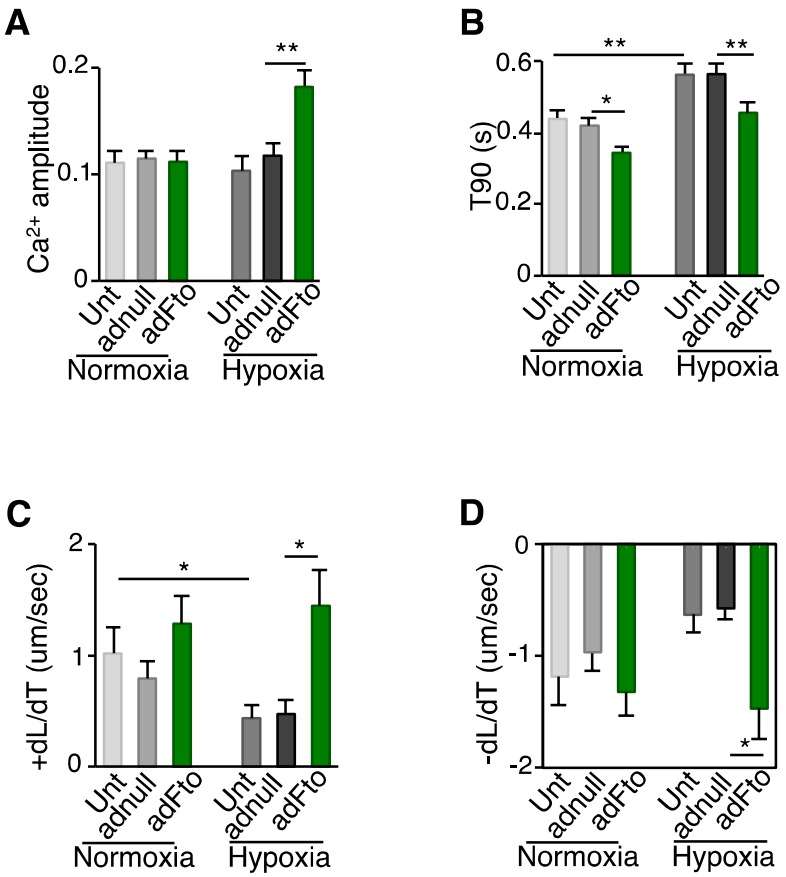

Supplemental Figure 5. Measurements of calcium and contractile properties in isolated adult rat primary cardiomyocytes. Measurements of **A,** Ca^{2+} amplitude, **B,** time to 90% decay, **C,** maximum sarcomere shortening velocity and **D,** minimum sarcomere shortening velocity in myocytes, n=23-74 cells per group from 4-12 rats. Sarcomere and Ca^{2+} transients were recorded at 1Hz pacing stimulation frequency with MyoPacer Field Stimulator (IonOptix MA, USA). Abbreviations, Unt: untreated; adnull: adenovirus with empty CMV promoter, adFto: adenovirus with full length Fto. Error bars represent SEM. **P*<0.05, ***P*<0.01, by one-way ANOVA.

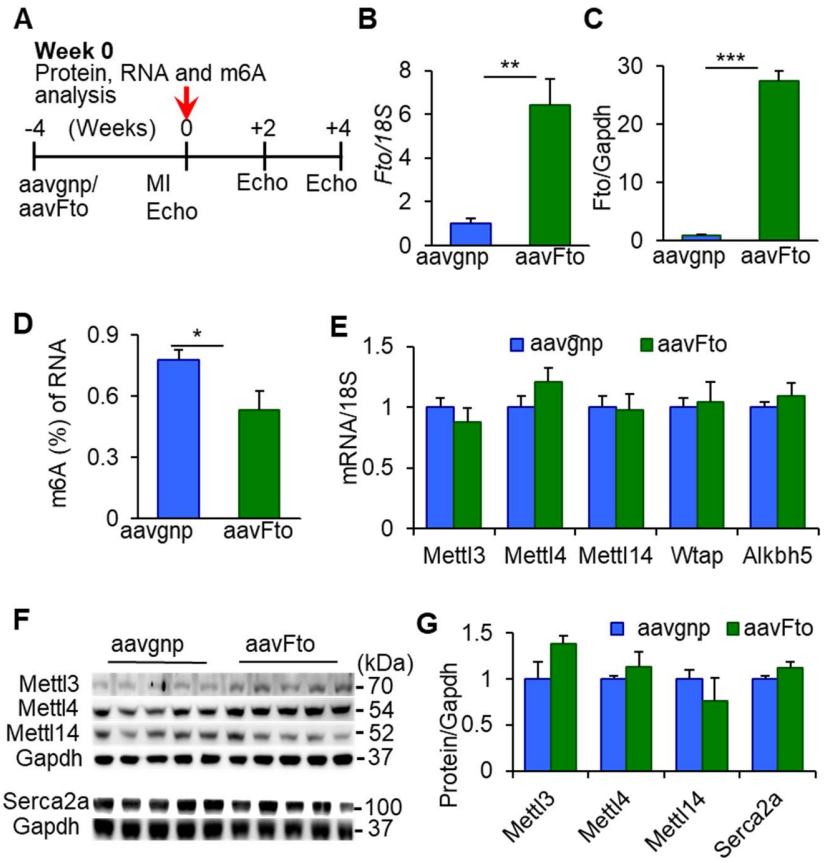

Supplemental Figure 6. Quantification of mRNA and protein at week 0 pre-MI surgery. A, design of aavFto study. **B**, Fto mRNA, n=4. **C**, Fto protein quantification from Fig. 4B, n=5. **D**, m6A quantification in total RNA, n=4-7. **E**, mRNA expression for selected m6A regulators, n=4. **F**, Representative immunoblots and **G**, densitometry quantification, n=5, for selected proteins. ***P*<0.01, ****P*<0.001

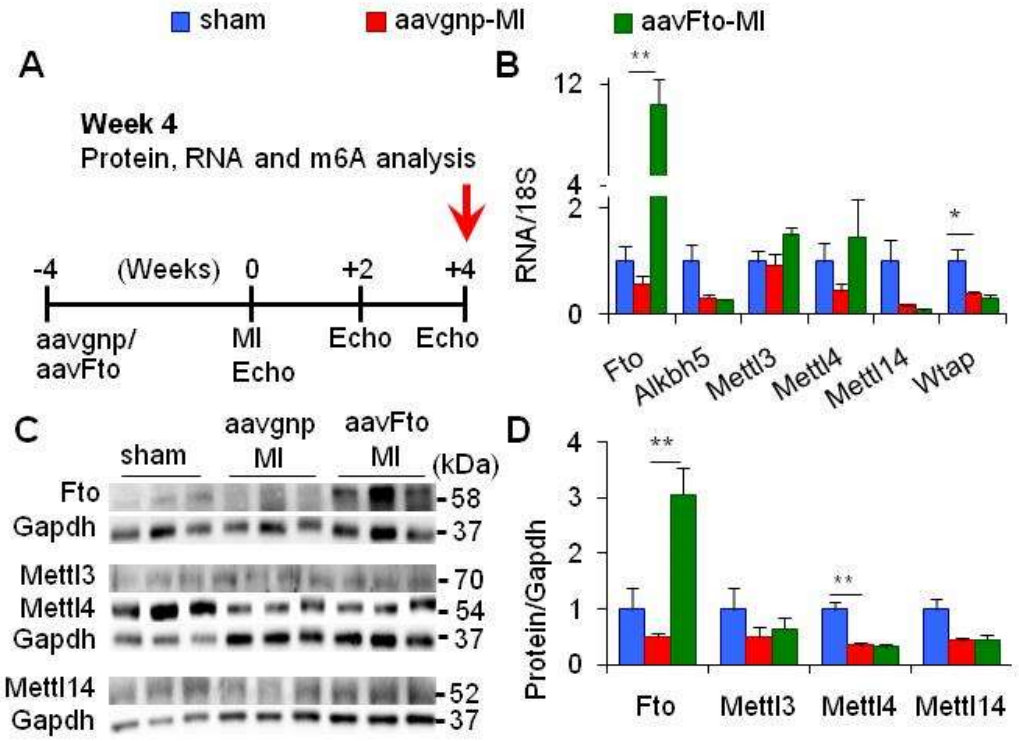

Supplemental Figure 7. Quantification of mRNA and protein at week 4 post-MI in AAV9 mice. A, design of aavFto study, **B**, mRNA for selected m6A regulators, n=4 **C**, Representative immunoblots for selected proteins and **D**, densitometry quantification, n=3-4, of selected proteins. Error bars represent SEM. **P*<0.05, ***P*<0.01, ****P*<0.001, by one-way ANOVA.

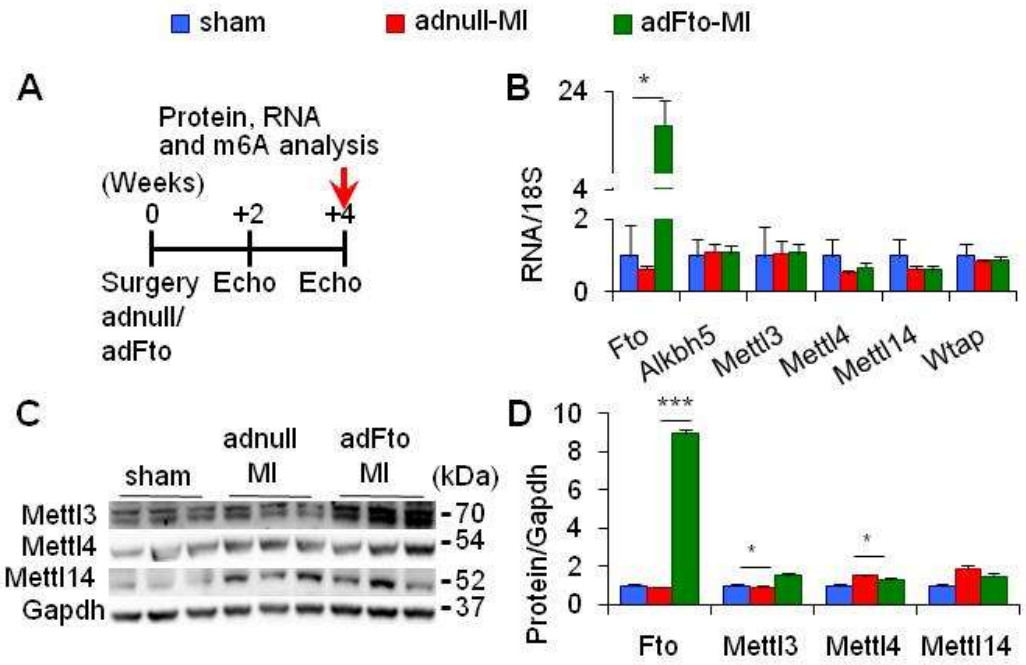

Supplemental Figure 8. Quantification of mRNA and protein at week 4 post-MI in adenovirus mice. A, design of adFto study. **B**, mRNA expression for selected m6A regulators, n=3-5. **C**, representative immunoblots for selected proteins and **D**, densitometry quantification (also for Fig. 5B), n=3-4, of selected proteins. Error bars represent SEM. **P*<0.05, ***P*<0.01, ****P*<0.001, by one-way ANOVA.

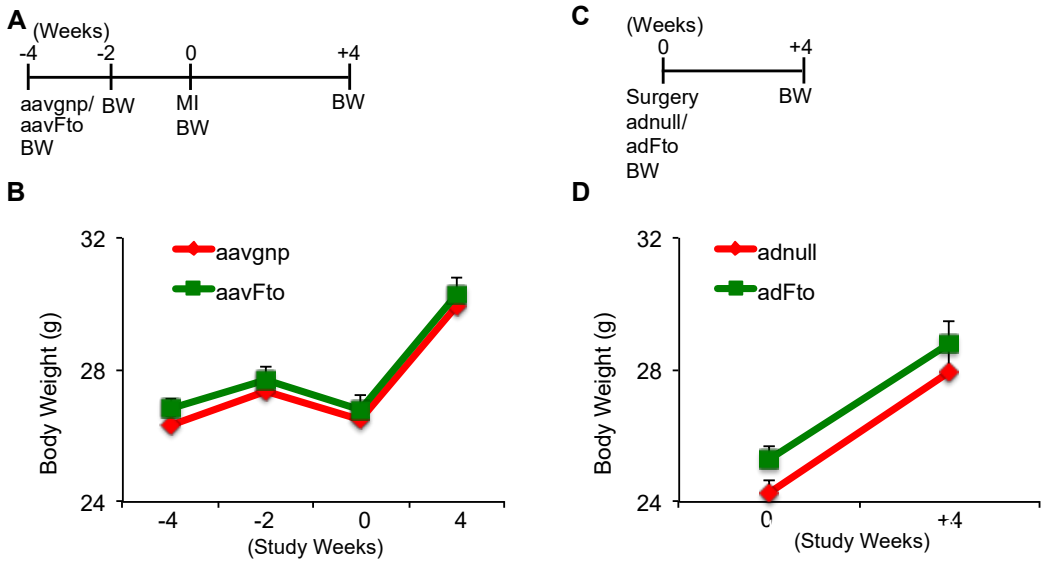

Supplemental Figure 9. Body weight measurements show no significant change between aavgnp/adnull and aavFto/adFto injected mice over study period. A, aavFto study design. **B**, Whole body weight measurements expressed as grams at -4, -2, 0 and 4 weeks, n=10-15 per group, **C**, adFto study design **D**, Whole body weight measurements expressed as grams at 0 and 4 weeks, n=8-12 per group. C57BL/6 mice, 10-14 weeks old (at the beginning of the experiments) were used. Error bars represent SEM.

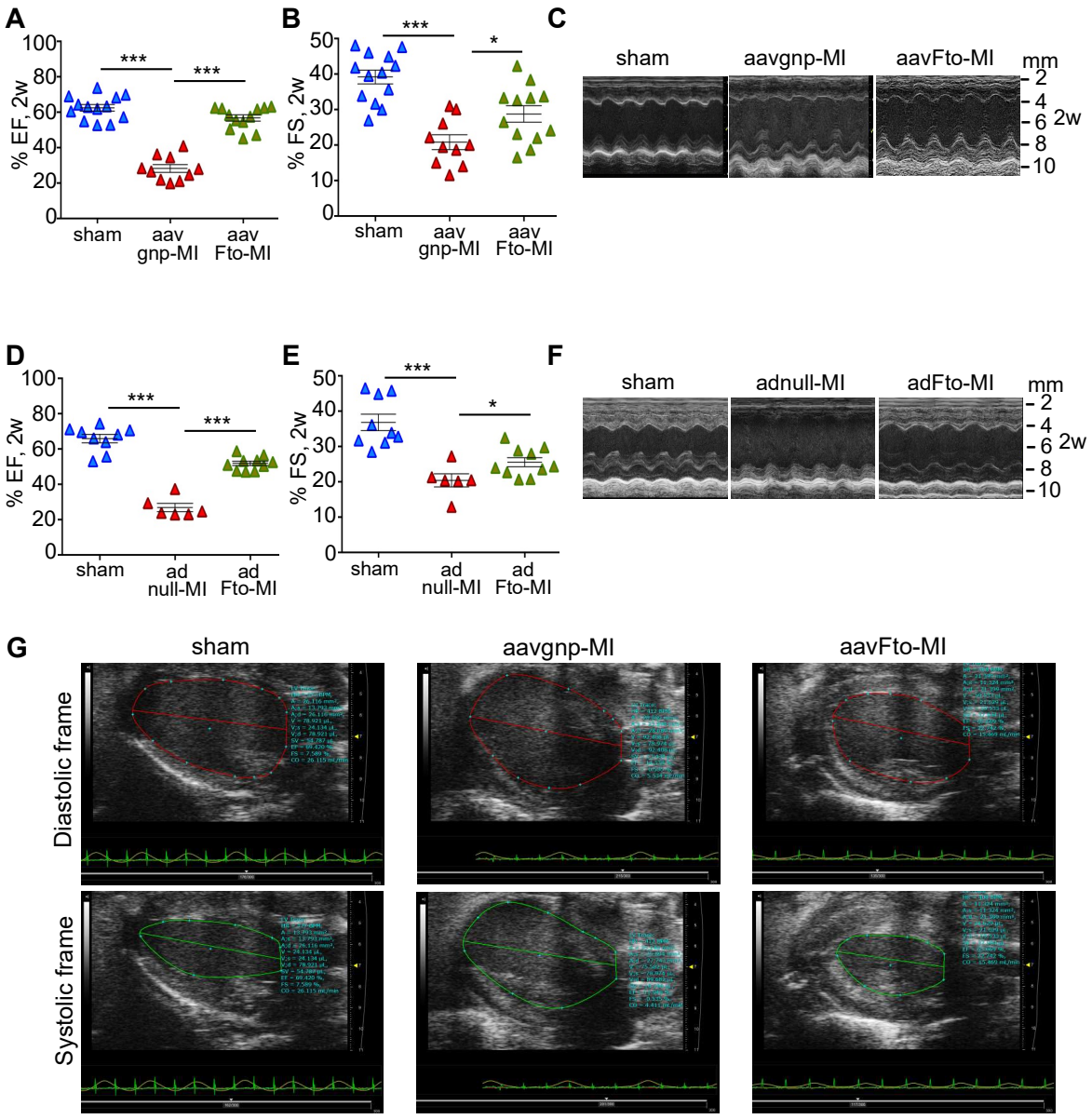

Supplemental Figure 10. Echocardiographic assessments in mouse post-MI. A, ejection fraction, **B**, fractional shortening and **C**, representative M-Mode echocardiograms showing anterior and posterior LV wall motion at 2w post-MI in aavgnp/aavFto mice. **D**, ejection fraction, **E**, fractional shortening and **F**, representative M-Mode echocardiograms showing anterior and posterior LV wall motion at 2w post-MI in adnull/adFto mice. **G,** An example of LV trace of parasternal long axis B-mode image (PSLAX) of mice heart in full diastole (red) and full systole (green). Error bars represent SEM. **P*<0.05, ****P*<0.001 by one-way ANOVA.

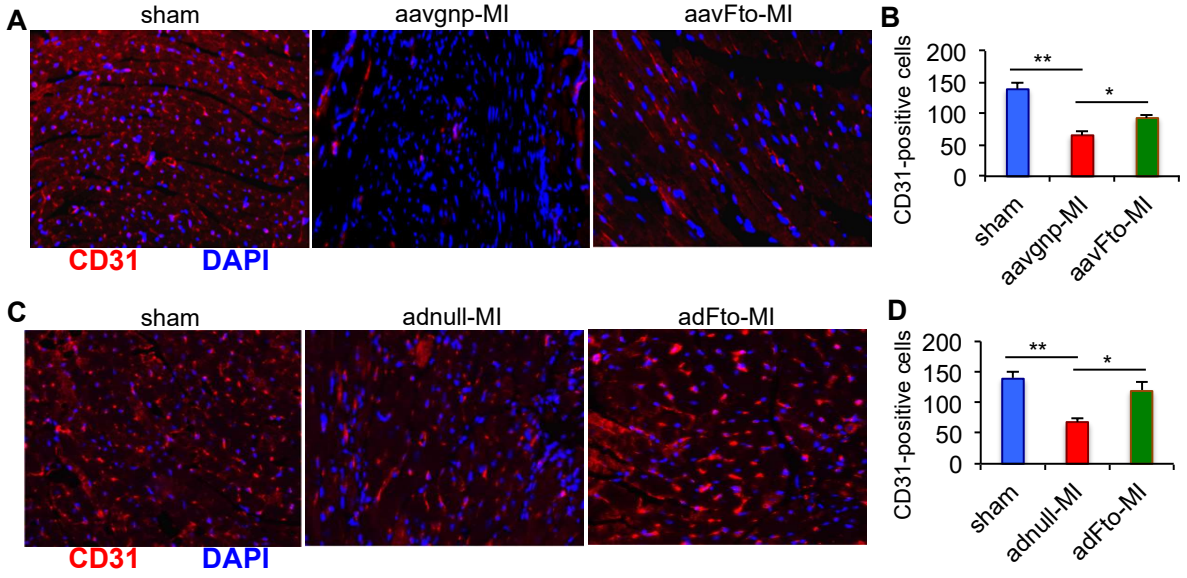

Supplemental Figure 11. CD31 Immunostaining in sham, MI (aav/adeno) and Fto injected mice. A, Representative immunostaining images showing CD31-positive cells in sham, aavgnp-MI and aavFto-MI mice at four weeks post surgeries. **B,** Quantification of CD31-positive cells in sham, aavgnp-MI and aavFto-MI mice at four weeks post surgeries; n=3 mice. **C,** Representative immunostaining images showing CD31-positive cells in sham, adnull-MI and adFto-MI mice at four weeks post surgeries. **D,** Quantification of CD31-positive cells in sham, adnull-MI and adFto-MI mice at four weeks post surgeries. Error bars represent SEM. **P*<0.05, ***P*<0.001.

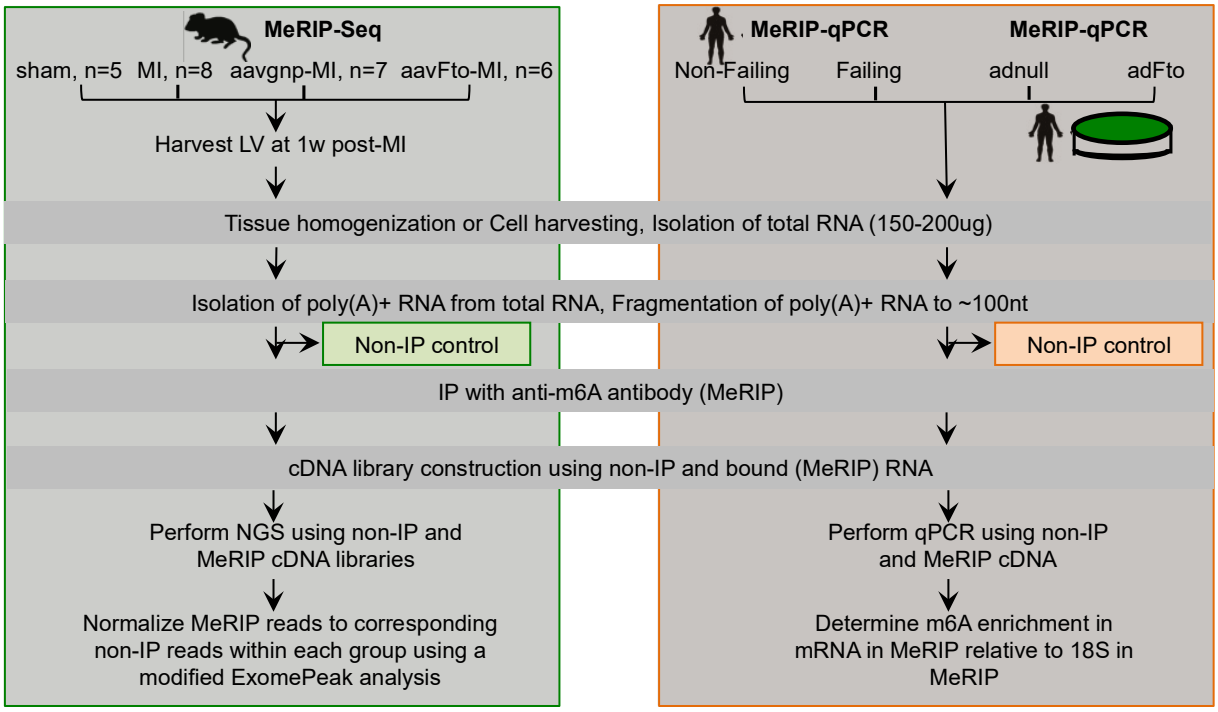

Supplemental Figure 12. Methods involving m6A-seq (MeRIP-seq) and qRT-PCR. Steps involved in Methylated (m6A) RNA immunoprecipitation and Next Generation Sequencing (MeRIP-Seq) and qPCR (MeRIP-qPCR). “n” indicates number of LVs (infarct area) pooled per MeRIP.

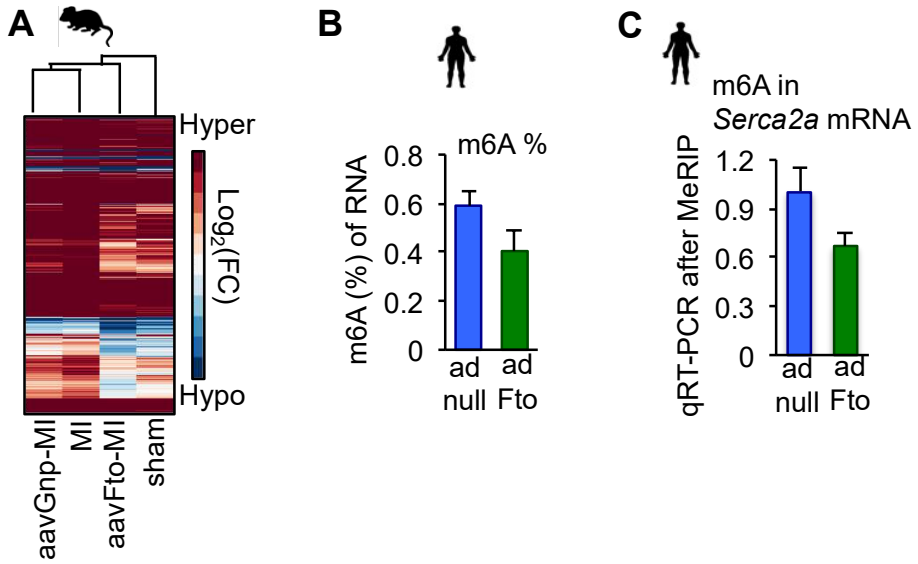

Supplemental Figure 13. MeRIP-seq in mice and MeRIP-qPCR in human myocytes. A, Heatmap/hierarchical clustering of Bound/non-IP total reads within each transcript. **B**, m6A % in total RNA, n=4, in human AC16 myocytes. **C**, MeRIP-qPCR quantification of m6A enrichment in *SERCA2A* mRNA in human AC16 myocytes, n=4. Error bars represent SEM

SUPPLEMENTAL REFERENCES

1. Chen J, Tung CH, Allport JR, Chen S, Weissleder R, Huang PL. Near-infrared fluorescent imaging of matrix metalloproteinase activity after myocardial infarction. Circulation. 2015; 111:1800-1805.

2. Kho C, Lee A, Jeong, D, Oh JG, Chaanine AH, Kizana E, Park WJ, Hajjar RJ. SUMO1-dependent modulation of SERCA2a in heart failure. Nature. 2011; 477:601-605.

3. Rapti K, Louis-Jeune V, Kohlbrenner E, Ishikawa K, Ladage D, Zolotukhin S, Hajjar RJ, Weber T. Neutralizing antibodies against AAV serotypes 1, 2, 6, and 9 in sera of commonly used animal models. Mol Ther. 2012; 20:73-83.

4. Langley SR, Dwyer J, Drozdov I, Yin X, Mayr M. Proteomics: from single molecules to biological pathways. Cardiovasc Res. 2013; 97:612-622.